

EVOLUTION OF PROTONEUTRON STARS

J.A. PONS^{1,2}, S. REDDY¹, M. PRAKASH¹, J.M. LATTIMER¹, and J.A. MIRALLES²

¹Department of Physics & Astronomy
SUNY at Stony Brook, Stony Brook, NY 11794-3800, USA

²Departament d'Astronomia i Astrofísica
Universitat de València, 46100 Burjassot, Spain

Received _____; accepted _____

arXiv:astro-ph/9807040v1 3 Jul 1998

ABSTRACT

We study the thermal and chemical evolution during the Kelvin-Helmholtz phase of the birth of a neutron star, employing neutrino opacities that are consistently calculated with the underlying equation of state (EOS). Expressions for the diffusion coefficients appropriate for general relativistic neutrino transport in the equilibrium diffusion approximation are derived. The diffusion coefficients are evaluated using a field-theoretical finite temperature EOS that includes the possible presence of hyperons. The variation of the diffusion coefficients is studied as a function of EOS and compositional parameters. We present results from numerical simulations of protoneutron star cooling for internal stellar properties as well as emitted neutrino energies and luminosities. We discuss the influence of the initial stellar model, the total mass, the underlying EOS, and the addition of hyperons on the evolution of the protoneutron star and upon the expected signal in terrestrial detectors.

We find that the differences in predicted luminosities and emitted neutrino energies do not depend much upon the details of the initial models or the underlying high-density EOS for early times ($t < 10$ s), provided that opacities are calculated consistently with the EOS. The same holds true for models which allow for the presence of hyperons, except when the initial mass is significantly larger than the maximum mass for cold, catalyzed matter. For times larger than about 10 seconds, and prior to the occurrence of neutrino transparency, the neutrino luminosities decay exponentially with a time constant that is sensitive to the high-density properties of matter. We also find the average emitted neutrino energy increases during the first 5 seconds of evolution, and then decreases nearly linearly with time. In general, increasing the protoneutron star mass increases the average energy and the luminosity of neutrinos, as well as the overall evolutionary time scale. The influence of hyperons or variations in the dense matter EOS is increasingly important at later times. *Metastable stars, those with hyperons which are unstable to collapse upon deleptonization, have relatively long evolution times, which increase the nearer the mass is to the maximum mass supported by a cold, deleptonized star.*

Subject headings: protoneutron star, neutrinos, supernova, stellar evolution

1. INTRODUCTION

A protoneutron (PNS) star forms in the aftermath of a successful supernova explosion as the stellar remnant becomes gravitationally decoupled from the expanding ejecta. The neutrinos radiated by the remnant are important to supernova energetics, and possibly are essential to supernova shock revival (Wilson 1985, Burrows, Hayes, & Fryxell 1995). They are also crucial to supernova nucleosynthesis, especially the r-process which may occur in the ejecta (Woosely et al. 1994). A careful study of the energies and time scales of neutrino emission in all flavors is also necessary for the interpretation of the data that will be recorded by terrestrial neutrino detectors in the event of a supernova occurring in our Galaxy or within several hundred kiloparsecs. In principle, observations of supernova neutrinos may not only allow an assessment of the remnant mass, but may also discriminate among competing types of equations of state (EOS) and internal neutron star compositions.

The essential microphysical ingredients that govern the macrophysical evolution of the PNS in the so-called Kelvin-Helmholtz epoch, during which the remnant changes from a hot and lepton-rich PNS to a cold and deleptonized neutron star, are the (EOS) of dense matter and its associated neutrino opacity. Among the characteristics of matter that widely vary among EOS models are their relative compressibilities (important in determining the theoretical neutron star maximum mass), symmetry energies (important in determining the typical stellar radius and in the relative n, p, e , and ν_e abundances) and specific heats (important in determining the local temperatures). These characteristics play important roles in determining the matter’s composition, in particular the possible presence of strange components (such as hyperons, a kaon condensate, or quark matter). These characteristics also significantly affect calculated neutrino opacities and diffusion time scales.

Immediately following the core bounce of a massive star, the PNS shrinks from more than 150 km in radius to less than 20 km as neutrino emission from the low-density outer few tenths of a solar mass of the star robs this region of pressure support. During this same period, from 0.1 s to 0.5 s, substantial accretion through the supernova’s shock also occurs, which adds mass and contributes significantly to the total neutrino emission. Nevertheless, both this stage and the much longer Kelvin-Helmholtz evolution which follows nearly fulfill the condition of hydrostatical equilibrium (Burrows & Lattimer 1986; henceforth BL in the text). The Kelvin-Helmholtz phase, which can last for several tens of seconds, consists of two major evolutionary stages. First, there is a *deleptonization stage* in which the excess trapped electron neutrinos diffuse from the central regions outward through the star. The diffusing neutrinos preferentially heat the stellar core while decreasing the net lepton and proton fractions. This stage is followed by an overall *cooling stage* in which the entropy in the star steadily decreases.

Since the work of BL, several authors (Burrows 1988;1990, Wilson & Mayle 1989,

Suzuki 1989, and Keil & Janka 1995) have performed numerical simulations of the cooling of a PNS. Our objective here is to improve upon these calculations by incorporating recent developments in the EOS of dense matter and neutrino interactions, and to perform a systematic study of the effects of varying the neutron star mass and the characteristics of the EOS. For this study, we will use the diffusion approximation for neutrino transport both because it provides a comparison to earlier works and because it allows us to easily assess how global characteristics of the neutrino emission such as average energies, integrated fluxes, and time scales change in response to various input parameters. This approach is sufficient to allow us to establish the connections between the microphysical ingredients and the duration of the deleptonization and cooling time scales, and to estimate the effects on neutrino signals. However, detailed simulations using a multigroup approach and more exact transport near the stellar surface will be necessary to calculate the emergent neutrino spectra precisely enough to make detailed predictions for current and future neutrino detectors. Such calculations are in progress.

Compared to the earlier works quoted above, several improvements are carried out in the neutrino transport scheme. These include

- (1) the development of the appropriate diffusion equations and a derivation of explicit expressions for the fluxes in terms of energy, temperature-, density-, and composition-dependent diffusion coefficients, which can be obtained from the reaction rates of neutrinos in matter. We present the calculations of these coefficients using the results of Reddy, Prakash, & Lattimer (1998) (henceforth RPL).
- (2) the development of a transport scheme that uses the appropriate energy-averaged diffusion coefficients.

The most important improvements in the EOS are that

- (1) the effects of finite entropy are calculated without approximation, and
- (2) the influence of the possible presence of strangeness in the form of hyperons is explored consistently.

We employ EOSs with more realistic compressibilities and high-density symmetry energies and nucleon effective masses as compared to BL. Keil & Janka (1995) (henceforth KJ) considered the consequences of having hyperons appear in the star, but with an approximate treatment of the effects of finite entropy and no modification to the opacities that reflected the presence of hyperons.

Several improvements over existing works are also made both in the calculation and in the implementation of neutrino opacities. The opacities are governed by charged current processes (absorption on baryons) and neutral current processes (scattering off baryons and electrons) in dense matter. The most significant of these improvements are:

- (1) an exact treatment of the kinematics of the neutrino-baryon and neutrino-electron

processes including the full effects of Pauli-blocking for arbitrary matter degeneracy, and (2) calculations of the effects of strong interactions arising from mass and energy shifts in a multicomponent system (including the presence of hyperons).

We have found that these improvements each tend to increase neutrino mean free paths (RPL), and, consequently, produce shorter emission time scales relative to the situation in which they are ignored.

In both BL and KJ, opacities were interpolated between expressions valid for a mixture of free Fermi gases in the degenerate and nondegenerate regimes, respectively. However, RPL demonstrated that interpolation can result in significant deviations from the exact phase-space integrals. RPL also showed that the exact phase-space integrals are relatively easy to compute, which obviates the need for interpolations.

The calculations of Suzuki (1989) employed free gas opacities from Bruenn (1985) which are valid when the matter is essentially non-degenerate and non-interacting. However, for the conditions of interest, neither of these conditions are generally satisfied. As discussed in RPL, this generally results in an underestimate of the neutrino mean free paths.

Furthermore, to include the effects of strong interactions, previous workers employed a constant, *i.e.*, density-, temperature-, and composition-independent, reduction factor multiplying the opacity. The effects of degeneracy and strong interactions on the opacities were not calculated consistently with the assumed underlying EOS.

In this paper, we focus on simulations of constant baryon mass and spherically symmetric protoneutron stars. We explicitly ignore effects due to accretion, rotation, magnetic fields and convection, which, in conjunction with multidimensional neutrino transport, may play an important role in the early evolution of the cores of protoneutron stars. In many current supernova models (Burrows 1988, Burrows & Goshy 1993), most accretion is completed within 0.5 s. In the constant baryon mass models we present here, it is assumed that the initial protoneutron star has a high-entropy mantle, so that the outer part of the star is initially at large radius. We find that it takes a few tenths of a second for the neutrinos in the high-entropy mantle to leak from the star and for the mantle to collapse to small radii. In effect, this largely simulates the effects of accretion on the protoneutron star’s evolution. We find that a large fraction of the star becomes connectively unstable after a few seconds. The omission of convection will likely lead to an underestimate of neutrino luminosities and average energies at these times, and should speed up protoneutron star cooling compared to our models. The inclusion of better treatments of accretion and the inclusion of convection will be studied in a later paper.

In §2, we develop the neutrino transport equations appropriate for the PNS problem by using the method of moments to solve the Boltzmann transport equations. These are simplified by employing the diffusion approximation, which results in expressions for the

number and energy fluxes in terms of energy, temperature-, density-, and composition-dependent diffusion coefficients. In §3, we describe the EOS employed in this paper, which is a finite-temperature, field-theoretical model in which the interactions among baryons are mediated by the exchange of σ , ω , and ρ mesons. It permits us to easily vary the matters' compressibility, symmetry energy, and baryonic specific heats, as well as allowing the systematic inclusion of hyperons, a kaon condensate, and/or quark matter. In §4, the opacities of matter are calculated using this EOS and the diffusion constants are determined. Our results for PNS evolutions are detailed in §5, in which we first describe a baseline simulation of a $1.6 M_{\odot}$ baryon mass, nucleonic EOS, PNS. We proceed to examine the consequences of varying the entropy and lepton content of the initial model, the inclusion of hyperons, and variations in the initial mass and the EOS. This section also contains a discussion of the expected luminosities and identification of connectively unstable zones. Our conclusions and outlook are contained in §6.

2. EVOLUTION EQUATIONS

2.1. Neutrino Transport Equations

The equations that govern the transport of energy and lepton number are obtained from the Boltzmann equation (BE) for massless particles given by (Lindquist 1966)

$$p^{\beta} \left(\frac{\partial f}{\partial x^{\beta}} - \Gamma_{\beta\gamma}^{\alpha} p^{\gamma} \frac{\partial f}{\partial p^{\alpha}} \right) = \left(\frac{df}{d\tau} \right)_{coll}, \quad (1)$$

where f is the invariant neutrino distribution function, p^{α} are the components of the neutrino 4-momentum with respect to the coordinate basis, $\Gamma_{\beta\gamma}^{\alpha}$ are the Christoffel symbols for the metric. (For the most part, we will use units setting $\hbar = 1$, $c = 1$). The indices α, β , and γ take the values t, r, θ , and Φ . The collision term on the right hand side is due to neutrino-matter interactions, and is most easily evaluated in a frame comoving with the matter. This entails rewriting the BE in terms of the 4-momentum components of the neutrino with respect to the matter p^a instead of the components in the coordinate basis. The comoving basis $\{\mathbf{e}_a\}$ satisfies $\mathbf{e}_a \cdot \mathbf{e}_b = \eta_{ab}$, with $\mathbf{e}_0 = \mathbf{u}$ representing the 4-velocity of matter. Using the metric

$$ds^2 = -e^{2\phi} dt^2 + e^{2\Lambda} dr^2 + r^2 d\theta^2 + r^2 \sin^2 \theta d\Phi^2, \quad (2)$$

and taking $\mathbf{u} = (\gamma e^{-\phi}, \gamma v e^{-\Lambda}, 0, 0)$, where v is the fluid velocity and the Lorentz factor $\gamma = (1 - v^2)^{-1/2}$, the BE in the comoving basis takes the form

$$p^b \left(e_b^{\beta} \frac{\partial f}{\partial x^{\beta}} - \Gamma_{bc}^a p^c \frac{\partial f}{\partial p^a} \right) = \left(\frac{df}{d\tau} \right)_{coll}, \quad (3)$$

where Γ_{bc}^a ($a, b, c \equiv 0, 1, 2, 3$) are the Ricci rotation coefficients. The non-zero Ricci coefficients in the spherically symmetric case are

$$\begin{aligned} \Gamma_{00}^1 = \Gamma_{01}^0 = e^{-\phi} e^{-\Lambda} \left(\frac{\partial(\gamma e^\phi)}{\partial r} + \frac{\partial(\gamma v e^\Lambda)}{\partial t} \right), \quad \Gamma_{11}^0 = \Gamma_{10}^1 = e^{-\phi} e^{-\Lambda} \left(\frac{\partial(\gamma e^\Lambda)}{\partial t} + \frac{\partial(\gamma v e^\phi)}{\partial r} \right), \\ \Gamma_{20}^2 = \Gamma_{22}^0 = \Gamma_{30}^3 = \Gamma_{33}^0 = -v\Gamma_{22}^1 = v\Gamma_{21}^2 = -v\Gamma_{33}^1 = v\Gamma_{31}^3 = \frac{\gamma v e^{-\Lambda}}{r}, \quad \Gamma_{33}^2 = -\Gamma_{32}^3 = -\frac{\cot \theta}{r}. \end{aligned} \quad (4)$$

The time t refers to that measured by an observer located at infinity. In spherical symmetry, the components of the neutrino 4-momentum are

$$p^a = \left(\omega, \omega\mu, \omega(1 - \mu^2)^{1/2} \cos \Phi, \omega(1 - \mu^2)^{1/2} \sin \Phi \right),$$

where μ is the cosine of the angle the neutrino momentum makes with respect to the radial direction and ω is the neutrino energy measured by a comoving observer. Then, the general relativistic BE in the spherically symmetric case reads (Thorne 1981)

$$\begin{aligned} \omega(e_0^t + \mu e_1^t) \frac{\partial f}{\partial t} + \omega(e_0^r + \mu e_1^r) \frac{\partial f}{\partial r} - \omega^2 \left(\mu \Gamma_{00}^1 + \mu^2 \Gamma_{10}^1 + (1 - \mu^2) \Gamma_{20}^2 \right) \frac{\partial f}{\partial \omega} \\ - \omega(1 - \mu^2) \left(\Gamma_{00}^1 + \Gamma_{22}^1 + \mu \Gamma_{10}^1 - \mu \Gamma_{20}^2 \right) \frac{\partial f}{\partial \mu} = \left(\frac{df}{d\tau} \right)_{coll}. \end{aligned} \quad (5)$$

A method often used to simplify the BE is to work with its angular moments (Thorne 1981). This is done by applying the operator

$$\frac{1}{2} \int_{-1}^{+1} d\mu \mu^i, \quad i = 0, 1, 2, \dots$$

to equation (5). Defining the i^{th} moment of the distribution function by

$$M_i = \frac{1}{2} \int_{-1}^{+1} d\mu \mu^i f,$$

the equations corresponding to the first two moments ($i = 0$ and 1) are:

$$\begin{aligned} \omega \left(e_0^t \frac{\partial M_0}{\partial t} + e_0^r \frac{\partial M_0}{\partial r} + e_1^t \frac{\partial M_1}{\partial t} + e_1^r \frac{\partial M_1}{\partial r} \right) \\ - \omega^2 \left(\Gamma_{00}^1 \frac{\partial M_1}{\partial \omega} + (\Gamma_{10}^1 - \Gamma_{20}^2) \frac{\partial M_2}{\partial \omega} + \Gamma_{20}^2 \frac{\partial M_0}{\partial \omega} \right) \\ + \omega \left((\Gamma_{10}^1 - \Gamma_{20}^2) (M_0 - 3M_2) - 2(\Gamma_{00}^1 + \Gamma_{22}^1) M_1 \right) = Q_0 \end{aligned} \quad (6)$$

$$\begin{aligned} \omega \left(e_0^t \frac{\partial M_1}{\partial t} + e_0^r \frac{\partial M_1}{\partial r} + e_1^t \frac{\partial M_2}{\partial t} + e_1^r \frac{\partial M_2}{\partial r} \right) \\ - \omega^2 \left(\Gamma_{00}^1 \frac{\partial M_2}{\partial \omega} + (\Gamma_{10}^1 - \Gamma_{20}^2) \frac{\partial M_3}{\partial \omega} + \Gamma_{20}^2 \frac{\partial M_1}{\partial \omega} \right) \\ + \omega \left(2(\Gamma_{10}^1 - \Gamma_{20}^2) (M_1 - 2M_3) + (\Gamma_{00}^1 + \Gamma_{22}^1) (M_0 - 3M_2) \right) = Q_1, \end{aligned} \quad (7)$$

where

$$Q_0 = \frac{1}{2} \int_{-1}^{+1} d\mu \left(\frac{df}{d\tau} \right)_{coll} \quad \text{and} \quad Q_1 = \frac{1}{2} \int_{-1}^{+1} d\mu \mu \left(\frac{df}{d\tau} \right)_{coll}. \quad (8)$$

Multiplying the 0th-moment equation (6) successively by $(\omega/2\pi^2)$ and $(\omega^2/2\pi^2)$, and integrating over the neutrino energy, one obtains the energy-averaged neutrino number and energy transport equations:

$$\begin{aligned} e_0^t \frac{\partial N_\nu}{\partial t} + e_0^r \frac{\partial N_\nu}{\partial r} + e_1^t \frac{\partial F_\nu}{\partial t} + e_1^r \frac{\partial F_\nu}{\partial r} \\ + (\Gamma_{10}^1 + 2\Gamma_{20}^2) N_\nu + (\Gamma_{00}^1 - 2\Gamma_{22}^1) F_\nu = S_N, \end{aligned} \quad (9)$$

$$\begin{aligned} e_0^t \frac{\partial J_\nu}{\partial t} + e_0^r \frac{\partial J_\nu}{\partial r} + e_1^t \frac{\partial H_\nu}{\partial t} + e_1^r \frac{\partial H_\nu}{\partial r} \\ + (\Gamma_{10}^1 + 3\Gamma_{20}^2) J_\nu + (2\Gamma_{00}^1 - 2\Gamma_{22}^1) H_\nu + (\Gamma_{10}^1 - \Gamma_{20}^2) P_\nu = S_E. \end{aligned} \quad (10)$$

Above,

$$N_\nu = \int_0^\infty \frac{d\omega}{2\pi^2} M_0 \omega^2, \quad F_\nu = \int_0^\infty \frac{d\omega}{2\pi^2} M_1 \omega^2, \quad S_N = \int_0^\infty \frac{d\omega}{2\pi^2} Q_0 \omega \quad (11)$$

$$J_\nu = \int_0^\infty \frac{d\omega}{2\pi^2} M_0 \omega^3, \quad H_\nu = \int_0^\infty \frac{d\omega}{2\pi^2} M_1 \omega^3, \quad P_\nu = \int_0^\infty \frac{d\omega}{2\pi^2} M_2 \omega^3, \quad S_E = \int_0^\infty \frac{d\omega}{2\pi^2} Q_0 \omega^2. \quad (12)$$

N_ν , F_ν , and S_N are the number density, number flux and number source term, respectively, while J_ν , H_ν , P_ν , and S_E are the neutrino energy density, energy flux, pressure, and the energy source term, respectively.

For spherically symmetric situations, equations (9) and (10) are the transport equations which contain full general relativistic effects including fluid velocity terms. These equations must be solved together with the hydrodynamical equations to study dynamical problems such as core collapse supernova. For the PNS problem, however, fluid velocities are small enough so that hydrostatic equilibrium is nearly fulfilled and the evolution is quasi-static.

Substituting Γ_{bc}^a in equations (9) and (10), and utilizing the continuity equation with the assumption of a quasi-static evolution (that is, neglecting terms of order v), we arrive at the well-known neutrino transport equations (BL) in a stationary metric in the form used so far in protoneutron star evolution:

$$\frac{\partial(N_\nu/n_B)}{\partial t} + \frac{\partial(e^\phi 4\pi r^2 F_\nu)}{\partial a} = e^\phi \frac{S_N}{n_B} \quad (13)$$

$$\frac{\partial(J_\nu/n_B)}{\partial t} + P_\nu \frac{\partial(1/n_B)}{\partial t} + e^{-\phi} \frac{\partial(e^{2\phi} 4\pi r^2 H_\nu)}{\partial a} = e^\phi \frac{S_E}{n_B}, \quad (14)$$

where n_B is the baryon number density and a is the enclosed baryon number inside a sphere of radius r .

2.2. The Equilibrium Diffusion Approximation

At high density and for temperatures above several MeV, the source terms Q_0 and Q_1 in equations (6) and (7) are sufficiently strong to ensure that neutrinos are in thermal and chemical equilibrium with the ambient matter. Thus, the neutrino distribution function in these regions is both nearly Fermi-Dirac and isotropic. We can approximate the distribution function as an expansion in terms of Legendre polynomials to $O(\mu)$, which is known as the diffusion approximation. Explicitly,

$$f(\omega, \mu) = f_0(\omega) + \mu f_1(\omega), \quad f_0 = [1 + e^{(\frac{\omega - \mu\nu}{kT})}]^{-1}, \quad (15)$$

where f_0 is the Fermi-Dirac distribution function at equilibrium ($T = T_{mat}$, $\mu_\nu = \mu_\nu^{eq}$), with ω and μ_ν being the neutrino energy and chemical potential, respectively.

The main goal is to obtain a relation for f_1 in terms of f_0 . In this approximation, the moments M_i of f which appear in equations (6) and (7) are

$$M_0 = f_0, \quad M_1 = \frac{1}{3}f_1, \quad M_2 = \frac{1}{3}f_0, \quad \text{and} \quad M_3 = \frac{1}{5}f_1. \quad (16)$$

We substitute these into equation (7) and again neglect all fluid velocity dependent terms (i.e., e_0^r , e_1^t , and Γ_{20}^2). Furthermore, since the transport is driven by slowly varying spatial gradients in temperature and chemical potential, the time derivative of f_1 has also been neglected. One then finds

$$e^{-\Lambda} \left(\frac{\partial f_0}{\partial r} - \omega \frac{\partial \phi}{\partial r} \frac{\partial f_0}{\partial \omega} \right) = 3 \frac{Q_1}{\omega}. \quad (17)$$

The interaction between neutrinos and matter is dominated by scattering (from both baryons and leptons), absorption (on baryons) and emission (due to electron capture) processes; thus the collision term Q_1 is given by

$$\left(\frac{df}{d\tau} \right)_{coll} = \omega \left(j_a(1-f) - \frac{f}{\lambda_a} + j_s(1-f) - \frac{f}{\lambda_s} \right), \quad (18)$$

where j_a is the emissivity, λ_a is the absorptivity, and j_s and λ_s represent the scattering contributions to the source term. These are

$$j_s = \frac{1}{(2\pi)^3} \int_0^\infty d\omega' \omega'^2 \int_{-1}^1 d\mu' \int_0^{2\pi} d\Phi f(\omega', \mu') R_s^{in}(\omega, \omega', \cos \theta), \quad (19)$$

$$\frac{1}{\lambda_s} = \frac{1}{(2\pi)^3} \int_0^\infty d\omega' \omega'^2 \int_{-1}^1 d\mu' \int_0^{2\pi} d\Phi [1 - f(\omega', \mu')] R_s^{out}(\omega, \omega', \cos \theta), \quad (20)$$

where θ is the angle between the ingoing and outgoing neutrino. From the reciprocity relations between a reaction rate and the rate of its inverse process (the principle of detailed

balance), the emissivities and absorptivities (R_s^{in} and R_s^{out} in the scattering kernels) are related according to

$$\frac{1}{\lambda_a(\omega)} = e^{\beta(\omega - \mu_\nu^{eq})} j_a(\omega) \quad \text{and} \quad R_s^{in} = e^{\beta(\omega' - \omega)} R_s^{out}. \quad (21)$$

The different elementary processes which contribute to equation (18) are described in §4.

To arrive at the final form for the diffusion equation and the appropriate definitions for the diffusion constants we expand the scattering kernel in terms of its Legendre moments:

$$R_l^{out} = \int_{-1}^1 d \cos \theta P_l(\cos \theta) R_s^{out}(\omega, \omega', \cos \theta). \quad (22)$$

Then, one finds

$$Q_0 = \omega \left(j_a(1 - f_0(\omega)) - \frac{f_0(\omega)}{\lambda_a} + \kappa_0^s \right) \quad , \quad Q_1 = -\omega \frac{f_1(\omega)}{3} \left(j_a + \frac{1}{\lambda_a} + \kappa_1^s \right), \quad (23)$$

where the scattering contributions to Q_0 and Q_1 are given by

$$\begin{aligned} \kappa_0^s = \frac{1}{(2\pi)^2} \int_0^\infty d\omega' \omega'^2 \left\{ [f_0(\omega') e^{\beta(\omega' - \omega)} - f_0(\omega) + (1 - e^{\beta(\omega' - \omega)}) f_0(\omega') f_0(\omega)] R_0^{out} \right. \\ \left. + (1 - e^{\beta(\omega' - \omega)}) \frac{f_1(\omega') f_1(\omega)}{9} R_1^{out} \right\}, \quad (24) \end{aligned}$$

$$\begin{aligned} \kappa_1^s = \frac{1}{(2\pi)^2} \int_0^\infty d\omega' \omega'^2 \left\{ [1 - f_0(\omega')(1 - e^{\beta(\omega' - \omega)})] R_0^{out} \right. \\ \left. - \frac{f_1(\omega')}{f_1(\omega)} [e^{\beta(\omega' - \omega)} + f_0(\omega)(1 - e^{\beta(\omega' - \omega)})] R_1^{out} \right\}. \quad (25) \end{aligned}$$

In the case that the scattering is isoenergetic, κ_1^s may be further simplified:

$$\kappa_1^s = \frac{\omega^2}{(2\pi)^2} \int_{-1}^1 d \cos \theta (1 - \cos \theta) R^{out}(\omega, \omega, \cos \theta), \quad (26)$$

which is the well-known *transport opacity* used in many applications. If we substitute the above expression for Q_1 into equation (17), we obtain the relation between f_0 and f_1 that we are looking for:

$$f_1 = -D(\omega) \left[e^{-\Lambda} \frac{\partial f_0}{\partial r} - \omega e^{-\Lambda} \frac{\partial \phi}{\partial r} \frac{\partial f_0}{\partial \omega} \right]. \quad (27)$$

The explicit form of the diffusion coefficient D appearing above is given by

$$D(\omega) = \left(j + \frac{1}{\lambda_a} + \kappa_1^s \right)^{-1}. \quad (28)$$

Because in most situations of interest to us neutrino scattering is dominated by scattering off baryons, the scattering processes are nearly elastic and the implicit dependence on f_1 in the diffusion coefficient may be safely ignored. However, should electron scattering or the inelastic contribution to baryon scattering become important, one is forced to solve a more complex integro-differential equation than the familiar Fick's law.

To obtain explicitly the equations that determine the lepton number and energy fluxes we note that

$$\frac{\partial f_0}{\partial r} = - \left(T \frac{\partial \eta_\nu}{\partial r} + \frac{\omega}{T} \frac{\partial T}{\partial r} \right) \frac{\partial f_0}{\partial \omega} , \quad (29)$$

where $\eta_\nu = \mu_\nu/T$ is the neutrino degeneracy parameter. Substituting the above relation in equation (27), we obtain

$$f_1 = -D(\omega)e^{-\Lambda} \left[T \frac{\partial \eta}{\partial r} + \frac{\omega}{T e^\phi} \frac{\partial (T e^\phi)}{\partial r} \right] \left(- \frac{\partial f_0}{\partial \omega} \right) . \quad (30)$$

In line with the definition of the fluxes given before in equations (11) and (12), the energy-integrated lepton and energy fluxes are

$$\begin{aligned} F_\nu &= - \frac{e^{-\Lambda} e^{-\phi} T^2}{6\pi^2} \left[D_3 \frac{\partial (T e^\phi)}{\partial r} + (T e^\phi) D_2 \frac{\partial \eta}{\partial r} \right] \\ H_\nu &= - \frac{e^{-\Lambda} e^{-\phi} T^3}{6\pi^2} \left[D_4 \frac{\partial (T e^\phi)}{\partial r} + (T e^\phi) D_3 \frac{\partial \eta}{\partial r} \right] . \end{aligned} \quad (31)$$

The coefficients D_2 , D_3 , and D_4 are related to the energy-dependent diffusion coefficient $D(\omega)$ through

$$D_n = \int_0^\infty dx x^n D(\omega) f_0(\omega) (1 - f_0(\omega)) , \quad (32)$$

where $x = \omega/T$. Note that these diffusion coefficients arise naturally from the transport equations. They depend only on the microphysics of the neutrino-matter interactions (see §4 for details). The fluxes appearing in the above equations are for one particle species. To include all six neutrino types, we redefine the diffusion coefficients in equation (31):

$$D_2 = D_2^{\nu_e} + D_2^{\bar{\nu}_e} , \quad D_3 = D_3^{\nu_e} - D_3^{\bar{\nu}_e} , \quad D_4 = D_4^{\nu_e} + D_4^{\bar{\nu}_e} + 4D_4^{\nu_\mu} . \quad (33)$$

2.3. Numerical Notes

We generally assume in this paper that the total baryon number in each simulation is conserved, that is, we do not include the effects of accretion. These effects will be incorporated in future work. The enclosed baryon number a is then a convenient Lagrangian

variable. The equations to be solved split naturally into a transport part, which has a strong time dependence, and a structure part, in which evolution is much slower. We choose to solve these two parts separately in an iterative fashion which is equivalent to solving them together.

Explicitly, the structure equations are

$$\frac{\partial r}{\partial a} = \frac{1}{4\pi r^2 n_B e^\Lambda}, \quad \frac{\partial m}{\partial a} = \frac{\rho}{n_B e^\Lambda} \quad (34)$$

$$\frac{\partial \phi}{\partial a} = \frac{e^\Lambda}{4\pi r^4 n_B} (m + 4\pi r^3 P), \quad \frac{\partial P}{\partial a} = -(\rho + P) \frac{e^\Lambda}{4\pi r^4 n_B} (m + 4\pi r^3 P). \quad (35)$$

The quantities m , ρ , and P include contributions from the leptons. To obtain the equations employed in the transport, we combine equation (13) and the corresponding equation for the electron fraction

$$\frac{\partial Y_e}{\partial t} = -e^\phi \frac{S_N}{n_B} \quad (36)$$

to obtain

$$\frac{\partial Y_L}{\partial t} + e^{-\phi} \frac{\partial(e^\phi 4\pi r^2 F_\nu)}{\partial a} = 0. \quad (37)$$

Similarly, we combine equation (14) with the matter energy equation

$$\frac{dU}{dt} + P \frac{d(1/n_B)}{dt} = -e^\phi \frac{S_E}{n_B}, \quad (38)$$

where U is the specific internal energy and use the first law of thermodynamics to obtain

$$e^\phi T \frac{\partial s}{\partial t} + e^\phi \mu_\nu \frac{\partial Y_L}{\partial t} + e^{-\phi} \frac{\partial e^{2\phi} 4\pi r^2 H_\nu}{\partial a} = 0. \quad (39)$$

In regions of small optical depth, diffusion codes can predict fluxes that exceed the black-body limit. To prevent this, we correct the fluxes by a flux limiter $3\Lambda(\xi)$, where $\xi_F = F_\nu/N_\nu$ and $\xi_H = H_\nu/J_\nu$ for the number and energy fluxes, respectively. For the functional form of $\Lambda(\xi)$, we tested both the Levermore & Pomraning (1981) and the Bowers & Wilson (1982) flux-limiters. Only the outermost few mass shells are affected by this choice, and we have not found it to make an appreciable difference in the overall evolution or in the mean neutrino energies or luminosities. For the PNS cooling problem, as long as most of the transport is nearly diffusive, small errors in the transport near the surface cannot affect the global evolution. This, however, is not the case in supernova simulations, in which the flux-limiter affects more of the computational grid and an appropriate treatment becomes a crucial aspect of transport.

The structure equations (34) and (35) satisfy the boundary conditions

$$\begin{aligned} r(a=0) &= 0; & m(a=0) &= 0, \\ \phi(a=a_s) &= \frac{1}{2} \log \left[1 - \frac{2m(a=a_s)}{r(a=a_s)} \right]; & P(a=a_s) &= P_s, \end{aligned} \quad (40)$$

where a_s is the total number of baryons in the star, which remains fixed during the evolution, and P_s is the surface pressure, which is chosen to be very small. We have checked that our results are insensitive to the exact value of P_s . The transport equations (37) and (39) also require boundary conditions. Both the energy and number fluxes must be zero at the center (this is equivalent to imposing null gradients of the temperature and chemical potential). At the surface, we may write

$$\xi_F = \alpha_n \quad \text{and} \quad \xi_H = \alpha_e, \quad (41)$$

where α_n and α_e are constants chosen to each be in the range 0.4 – 0.6. The results for overall neutrino number and energy fluxes are insensitive to the exact choice of these constants, due to the fact that the fluxes saturate near the surface and the values of Y_ν in the surface region adjusts itself to compensate for small changes in α_n and α_e .

An initial model is specified by choosing entropy s and lepton fraction Y_L profiles in a and relaxing the star to hydrostatic equilibrium, which determines values for the radius r , gravitational mass m , gravitational potential ϕ , and pressure P . In general, this initial model will not be in radiative equilibrium; however, we found that radiative equilibrium is established within about 5 ms, a time too short to be important for the protoneutron star evolution.

The evolution is begun by taking an initial transport time step, determining the quantities $Y'_L(a)$ and $s'(a)$ as first estimates for the lepton fraction and entropy at the end of the time step. In this step, the radius, gravitational mass and pressure profiles are kept fixed. Now using these values of lepton number $Y'_L(a)$ and entropy $s'(a)$, we solve the structural equations relaxing the star into hydrostatic equilibrium, which determines $r'(a)$, $m'(a)$, $\phi'(a)$, and $P'(a)$. Using these primed values for r, m, ϕ , and P , but the original values of $s(a)$ and $Y_L(a)$, we retake the transport time step, thereby determining updated estimates, $s''(a)$ and $Y''_L(a)$. This is followed by another hydrostatic equilibrium relaxation which determines $r''(a)$, $m''(a)$, $\phi''(a)$, and $P''(a)$. This iterative procedure is found to converge rapidly, typically in 3-4 iterations. This method is equivalent to using a full implicit discretization scheme to solve the structure and transport equations simultaneously.

2.4. Neutrino Luminosities

The ultimate objective of an observation of neutrinos from a Galactic supernova will be to deduce the properties of the PNS, including its mass, composition, and the EOS. The prediction of neutrino signals, and the determination of how well the mass and properties of the EOS can be estimated from them, is an important goal of our work. The signal depends both upon the neutrino fluxes and energy spectra. Its accurate determination requires the use of better transport than the diffusive, approach used in this paper. Thus, we have limited our predictions to those utilizing information only from the total neutrino luminosity and the average emitted energy of all neutrinos. However, our neutrino transport calculations tracked each flavor of neutrino and the diffusion constants were defined appropriately. In fact, detailed transport calculations show that the emitted spectra are, to a fair approximation, Fermi-Dirac with a small effective degeneracy parameter for all flavors of neutrinos (Mayle, Wilson, & Schramm 1987). Furthermore, the presence of a small degeneracy parameter gives negligible corrections to a detector’s count rate (Lattimer & Yahil 1989). Thus, a fair representation of the signal in a terrestrial detector can be found from the time dependence of the total neutrino luminosity and average neutrino energy together with an assumption of a Fermi-Dirac spectrum with zero chemical potential.

The total neutrino luminosity is the time rate of change of the star’s gravitational mass, and is therefore primarily a global property of the evolution. This luminosity, due to energy conservation, must also equal

$$L_\nu = e^{2\phi} 4\pi r^2 H_\nu \quad (42)$$

at the edge of the star. We have checked this test of energy conservation for our code and find that it is valid to better than 1% at all times greater than about 5 ms, when the star comes into radiative equilibrium. For times greater than about 5 ms, initial transients become quite small and the predicted luminosities should be relatively accurate compared to full transport simulation. We estimate the average energy of neutrinos from the temperature T_ν of the matter at the neutrinosphere R_ν , defined to be the location in the star where the flux factor $\xi_H = 0.25$. However, since the spectrum may not be Fermi-Dirac at the neutrinosphere, our transport scheme cannot give a very precise value for the average energy. Comparing with better transport in this region, we find that the average energy $\langle E_\nu \rangle \approx 3T_\nu$, where T_ν is a mass average in the outermost zone. Because it is a globally determined quantity, the luminosity L_ν is necessarily more accurately determined than either R_ν or T_ν . In lieu of more complete transport results, we will place more weight on L_ν in the estimate of detector signals in §5.7.

3. THE EQUATION OF STATE

The role of the EOS in determining the structure of neutron stars has been studied extensively (see, for example, Prakash et al. 1997 & references therein). The masses and radii of neutron stars depend upon the matters' compressibility, the composition of matter at high density, and the nuclear symmetry energy. In the PNS problem, the finite temperature aspects of the EOS also play an important role. During the early evolution the entropy in the central regions is moderately high $s \sim 1 - 2$, which correspond to temperatures in the range $T = 20 - 50$ MeV. In this work we employ a finite temperature field-theoretical model where the interactions between baryons are mediated by the exchange of σ, ω , and ρ mesons. Including the leptonic contributions, the total Lagrangian density is given by (Serot & Walecka 1992),

$$\begin{aligned} L &= L_\ell + L_H \\ &= \sum_l \bar{l}(-i\gamma^\mu \partial_\mu - m_l)l + \sum_i \bar{B}_i(-i\gamma^\mu \partial_\mu - g_{\omega i}\gamma^\mu \omega_\mu - g_{\rho i}\gamma^\mu \mathbf{b}_\mu \cdot \mathbf{t} - M_i + g_{\sigma i}\sigma)B_i \\ &\quad - \frac{1}{4}W_{\mu\nu}W^{\mu\nu} + \frac{1}{2}m_\omega^2\omega_\mu\omega^\mu - \frac{1}{4}\mathbf{B}_{\mu\nu}\mathbf{B}^{\mu\nu} + \frac{1}{2}m_\rho^2b_\mu b^\mu + \frac{1}{2}\partial_\mu\sigma\partial^\mu\sigma - \frac{1}{2}m_\sigma^2\sigma^2 - U(\sigma) \end{aligned} \quad (43)$$

Here, the leptons, $l = e^-$ and μ^- , and B are the Dirac spinors for baryons and \mathbf{t} is the isospin operator. The sums include baryons $i = n, p, \Lambda, \Sigma$, and Ξ . The field strength tensors for the ω and ρ mesons are $W_{\mu\nu} = \partial_\mu\omega_\nu - \partial_\nu\omega_\mu$ and $\mathbf{B}_{\mu\nu} = \partial_\mu\mathbf{b}_\nu - \partial_\nu\mathbf{b}_\mu$, respectively. The potential $U(\sigma)$ represents the self-interactions of the scalar field and is taken to be of the form

$$U(\sigma) = \frac{1}{3}bM_n(g_{\sigma N}\sigma)^3 + \frac{1}{4}c(g_{\sigma N}\sigma)^4. \quad (44)$$

Electrons and muons are included in the model as noninteracting particles, since their interactions give small contributions compared to those of their free Fermi gas parts.

In the mean field approximation, the partition function (denoted by Z_H) for the hadronic degrees of freedom is given by

$$\ln Z_H = \beta V \left[\frac{1}{2}m_\omega^2\omega_0^2 + \frac{1}{2}m_\rho^2b_0^2 - \frac{1}{2}m_\sigma^2\sigma^2 - U(\sigma) \right] + 2V \sum_i \int \frac{d^3k}{(2\pi)^3} \ln \left(1 + e^{-\beta(E_i^* - \nu_i)} \right), \quad (45)$$

where $\beta = T^{-1}$ and V is the volume (we take $k_B = 1$). The contribution of antibaryons is not significant for the thermodynamics of interest here, but is straightforwardly included in equation (45). Here, the effective baryon masses $M_i^* = M_i - g_{\sigma i}\sigma$ and $E_i^* = \sqrt{k^2 + M_i^{*2}}$. The chemical potentials are given by

$$\mu_i = \nu_i + g_{\omega i}\omega_0 + g_{\rho i}t_{3i}b_0, \quad (46)$$

where t_{3i} is the third component of isospin for the baryon. Note that particles with $t_{3i} = 0$, such as the Λ and Σ^0 do not couple to the ρ . The effective chemical potential ν_i sets the scale of the temperature dependence of the thermodynamical functions.

Using Z_H , the thermodynamic quantities can be obtained in the standard way. The pressure $P_H = TV^{-1} \ln Z_H$, the number density for species B , and the energy density ε_H are given by

$$\begin{aligned} n_i &= 2 \int \frac{d^3k}{(2\pi)^3} \left(e^{\beta(E_i^* - \nu_i)} + 1 \right)^{-1} , \\ \varepsilon_H &= \frac{1}{2} m_\sigma^2 \sigma^2 + U(\sigma) + \frac{1}{2} m_\omega^2 \omega_0^2 + \frac{1}{2} m_\rho^2 b_0^2 + 2 \sum_i \int \frac{d^3k}{(2\pi)^3} E_i^* \left(e^{\beta(E_i^* - \nu_i)} + 1 \right)^{-1} . \end{aligned} \quad (47)$$

The entropy density is then given by $s_H = \beta(\varepsilon_H + P_H - \sum_i \mu_i n_i)$. The meson fields are obtained by extremization of the partition function, which yields the equations

$$\begin{aligned} m_\omega^2 \omega_0 &= \sum_i g_{\omega i} n_i \quad ; \quad m_\rho^2 b_0 = \sum_i g_{\rho i} t_{3B} n_i , \\ m_\sigma^2 \sigma &= -\frac{dU(\sigma)}{d\sigma} + \sum_i g_{\sigma i} \quad 2 \int \frac{d^3k}{(2\pi)^3} \frac{M_i^*}{E_i^*} \left(e^{\beta(E_i^* - \nu_i)} + 1 \right)^{-1} . \end{aligned} \quad (48)$$

The total partition function $Z_{total} = Z_H Z_L$, where Z_L is the standard noninteracting partition function of the leptons. The additional conditions needed to obtain a solution are provided by the charge neutrality requirement, and, when neutrinos are not trapped, the set of equilibrium chemical potential relations required by the general condition

$$\mu_i = b_i \mu_n - q_i \mu_l , \quad (49)$$

where b_i is the baryon number of particle i and q_i is its charge. For example, when $\ell = e^-$, this implies the equalities

$$\mu_\Lambda = \mu_{\Sigma^0} = \mu_{\Xi^0} = \mu_n , \quad \mu_{\Sigma^-} = \mu_{\Xi^-} = \mu_n + \mu_e , \quad \text{and} \quad \mu_p = \mu_{\Sigma^+} = \mu_n - \mu_e . \quad (50)$$

In the case that the neutrinos are trapped, equation (49) is replaced by

$$\mu_i = b_i \mu_n - q_i (\mu_l - \mu_{\nu_\ell}) . \quad (51)$$

The new equalities are then obtained by the replacement $\mu_e \rightarrow \mu_e - \mu_{\nu_e}$ in equation (50). The introduction of additional variables, the neutrino chemical potentials, requires additional constraints, which we supply by fixing the lepton fractions, $Y_{L\ell}$, appropriate for conditions prevailing in the evolution of the protoneutron star. The contribution to pressure from neutrinos of a given species is given by their free Fermi gas expressions.

In the nucleon sector, the constants $g_{\sigma N}, g_{\omega N}, g_{\rho N}, b$, and c are determined by reproducing the nuclear matter equilibrium density n_0 , and the binding energy per nucleon,

the symmetry energy, the compression modulus K_0 , and the nucleon Dirac effective mass M^* at n_0 . The parameters of the models are listed in Table 1 and for the most part are taken from Glendenning & Moszkowski (1991). Model GM1 is a stiff EOS ($K_0 = 300$ MeV) while the model GM3 is softer with $K_0 = 240$ MeV. To study the possible role played by the nuclear symmetry energy we also investigate the model GM4, which is similar to GM3 but with a smaller symmetry energy.

In addition to models containing only nucleonic degrees of freedom (GM1np & GM3np) we investigate models that allow for the presence of hyperons (GM1npH & GM3npH). The hyperon coupling constants may be determined by reproducing the binding energy of the Λ hyperon in nuclear matter (Glendenning & Moszkowski 1991). Parameterizing the hyperon-meson couplings in terms of nucleon-meson couplings through

$$x_{\sigma H} = g_{\sigma H}/g_{\sigma N}, \quad x_{\omega H} = g_{\omega H}/g_{\omega N}, \quad x_{\rho H} = g_{\rho H}/g_{\rho N}, \quad (52)$$

the Λ binding energy at nuclear density is given by

$$(B/A)_\Lambda = -28 = x_{\omega\Lambda}g_{\omega N}\omega_0 - x_{\sigma\Lambda}g_{\sigma N}\sigma_0, \quad (53)$$

in units of MeV. Thus, a particular choice of $x_{\sigma\Lambda}$ determines $x_{\omega\Lambda}$ uniquely. To keep the number of parameters small, the coupling constant ratios for all the different hyperons are assumed to be the same. In model GM1, the hyperon couplings are given by

$$x_\sigma = x_{\sigma\Lambda} = x_{\sigma\Sigma} = x_{\sigma\Xi} = 0.6, \quad \text{and} \quad x_\omega = x_{\omega\Lambda} = x_{\omega\Sigma} = x_{\omega\Xi} = 0.653. \quad (54)$$

The ρ -coupling is of less consequence and is taken to be of similar order, i.e. $x_\rho = x_\sigma$. In GM3, $x_\sigma = 0.6$, $x_\omega = 0.659$ and $x_\rho = 0.6$.

In Figure 1 the particle fractions for models GM3np and GM3npH are shown with and without trapped neutrinos. The left panels show the particle fractions in hot and neutrino-free matter (mimics the ambient conditions subsequent to deleptonization) and the right panels show the particle fractions in neutrino trapped matter (ambient conditions in the core at birth). Considering matter with nucleons-only first, note that the major effect of trapping is to make the electron (and hence the proton) concentration high compared to the case in which matter is neutrino free. Compared to the free gas case the proton fraction is appreciably larger in matter with strong interactions due to the larger symmetry energies. At fixed Y_L , this acts to decrease the electron neutrino fraction at high density (see top right panel). During the deleptonization phase, the EOS affects the evolution mainly through the density dependent nuclear symmetry energy as it directly influences λ_{ν_e} (see §4) and the magnitude of the spatial gradient $\partial\mu_\nu/\partial r$ (see §2). Subsequent to deleptonization, the proton fractions decreases, but is still high enough to enable the charged current reactions to occur for most relevant densities and temperatures of interest (see §4).

Although the threshold densities for the appearance of hyperons are sensitive to the hyperon coupling constants (Knorren, Prakash, & Ellis 1997), the higher entropies encountered during the early evolution generally results in hyperon fractions which are larger compared to the case of zero temperature matter (bottom left panel). In lepton-rich matter (bottom right panel), the appearance of hyperons is delayed to higher densities due to the relative dispositions of the various chemical potentials. With the appearance of the hyperons, the neutrino population begins to increase with density, in contrast to the monotonic decrease exhibited in the hyperon free case. Since the negatively charged hyperons effectively replace the electrons at high density, the final lepton content of stars with hyperons is smaller relative to those in nucleons-only matter. Correspondingly, we should expect to see a larger lepton number radiated from stars with hyperons (see §5).

In Figure 2 the variation of pressure with baryon density is shown. The upper panels show the results for $s = 2$ and the lower panels for $s = 1$. Thermal effects contribute only modestly to the total pressure. The pressure is dominated from effects of interactions and degeneracy at high density. The left panels in Figure 2 show results for $Y_{\nu_e} = 0$, and the right panels for a fixed lepton fraction of $Y_L = 0.4$. While the differences between lepton rich and lepton poor matter for the np models are negligible, significant differences arise in models with hyperons. When the electron neutrino fraction is large, their presence inhibits the appearance of hyperons (see also Figure 1; note however, that a large hyperonic component at high density in the neutrino free case significantly softens the EOS (Prakash et al. 1997)). This softening with decreasing lepton number will lead to compression during the deleptonization epoch. Hence, there exists a window of initial masses for which the star becomes unstable to gravitational collapse during deleptonization. The maximum masses supported at low temperature and for lepton poor matter are significantly smaller than for hot and lepton rich matter.

Finite temperature properties of matter at high density influence the diffusion of neutrinos especially through the specific heat. Neutrino mean free paths are strongly temperature dependent (see §4) and the ambient matter temperature controls the diffusion of neutrinos to a large extent. In Figure 3, we show the matter temperature at fixed entropy per baryon as a function of the baryon density to contrast the behavior observed in models with and without hyperons. The trends observed in the np models are similar while the differences between np and npH models are very significant. The appearance of additional fermionic degrees of freedom in the form of hyperons (we may expect similar behavior in models with quarks (Prakash, Cooke, & Lattimer 1995)) increases the low temperature specific heat. This generally favors lower temperatures during the evolution for the npH models, all else being equal. This is because, in charge neutral and beta-equilibrated matter, bulk of the entropy resides in the baryons (Prakash et al. 1997). Under degenerate situations ($T/E_{F_i} \gg 1$), this result may be understood from the relation that connects the

temperature and baryonic entropy (or specific heat) through the concentrations ($Y_i = n_i/n$):

$$\frac{\pi^2 T}{s} = \frac{(3\pi^2 n_B)^{2/3}}{\sum_i Y_i^{1/3} \sqrt{M_i^{*2} + k_{F_i}^2}} \Rightarrow \begin{cases} \frac{(3\pi^2 n_B)^{2/3}}{\sum_i Y_i^{1/3} M_i^*} & \text{for } M_i^* \gg k_{F_i} \\ \frac{(3\pi^2 n_B)^{1/3}}{\sum_i Y_i^{2/3}} & \text{for } M_i^* \ll k_{F_i}, \end{cases} \quad (55)$$

where $k_{F_i} = (3\pi^2 n_B Y_i)^{2/3}$ are the Fermi momenta. For the temperatures of interest here, and particularly with increasing density, the above relation provides an accurate representation of the exact results for entropies per baryon even up to $s = 2$. The behavior with density of both the concentrations and effective masses controls the temperatures for a fixed s . In the absence of any variation with M_i^* , a system with more components at a given baryon density has a smaller temperature than a system with fewer components (recall that $\sum_i Y_i = 1$). Effective masses that rapidly drop with density oppose this behavior and lead to larger temperatures. The fact that the temperatures are smaller in the presence of hyperons than those in nucleons-only matter attests to the predominant effect of concentrations. Note that the differences between the temperatures for the cases with and without hyperons are larger than those obtained by using different models for the individual cases.

However, as we have seen from Figure 2, the appearance of hyperons also leads to higher central densities due to softening; this acts to compensate for the higher specific heat in npH models. In addition, the larger neutrino chemical potentials (see Figure 4) in npH models generate larger entropies during the deleptonization epoch; this also acts to increase the central temperature in these models. Results discussed in §5 clearly show that despite the significant differences seen in Figure 3 the maximum central temperatures reached in the both np and npH models are nearly equal due to the above mentioned feedbacks.

The lepton chemical potentials influence the deleptonization epoch (see §5) and are shown in Figure 4. For np models a lower nuclear symmetry energy favors a larger ν_e fraction and has little effect on the e^- fraction at $Y_l = 0.4$. Models with hyperons lead to significantly larger μ_{ν_e} and lower μ_e , both of which influence the diffusion of electron neutrinos. The electron chemical potentials in neutrino free matter are reduced to a greater extent by changes in composition and symmetry energy as there are no neutrinos to compensate for changes in $\hat{\mu} = \mu_n - \mu_p$. The impact these modifications will have on the evolution are discussed in §5.

We turn now to some aspects of the global energetics. The binding energy, which is the difference between baryonic and gravitational masses, is an important observational parameter because nearly 99% of it appears as radiated neutrino energy. The rate of change of binding is essentially the total neutrino luminosity. In Figure 5, we display the binding energy as a function the baryonic mass for the models considered here. As found by Lattimer & Yahil (1989) and Prakash et al. (1997), there exists a universal empirical

relationship between the binding energy and the mass:

$$B.E. = (M_B - M_G)c^2 \simeq (0.065 \pm 0.01) \left(\frac{M_B}{M_\odot} \right)^2 M_\odot. \quad (56)$$

This universality is not altered by the presence of significant softening due to the presence of hyperons, kaons or quarks. Since nearly all of the binding energy is released in the form of neutrinos, *an accurate measurement of the total neutrino energy will lead to a good estimate of the remnant mass*. However, as the results of Figure 5 show, it will not be possible to distinguish the various EOSs from the total binding energy alone.

Table 2 shows the maximum gravitational masses for the models studied. The three columns roughly depict the three important stages of the evolution of a protoneutron star. At birth the PNS has $s = 1$ and $Y_L = 0.4$, after deleptonization the entropy has reached its maximum ($s \sim 2$), and finally cools down to its final cold catalyzed state.

4. NEUTRINO-MATTER INTERACTION RATES

One of the important microphysical inputs in PNS simulations is the neutrino opacity at supra-nuclear density (Bruenn 1985; Mezacappa & Bruenn 1993; Burrows & Lattimer 1986; Wilson & Mayle 1989; Suzuki & Sato 1992; Keil 1994; Keil & Janka 1995). However, calculations of neutrino opacities in dense matter have received relatively little attention compared to other physical inputs such as the EOS. Although it was realized over a decade ago that the effects due to degeneracy and strong interactions significantly alter the neutrino mean free paths, it is only recently that detailed calculations have become available (Reddy & Prakash 1997; RPL 1998; Reddy et al. 1997, Prakash & Reddy 1997, Burrows & Sawyer, 1998a,b). The weak interaction rates in hot and dense matter are modified due to many in-medium effects. The most important of these are:

- (1) *Composition*: The neutrino mean free paths depend sensitively on the composition which is sensitive to the nature of strong interactions. First, the different degeneracies of the different Fermions determines the single-pair response due to Pauli blocking. Second, neutrinos couple differently to different baryonic species; consequently, the net rates will depend on the individual concentrations.
- (2) *In-medium dispersion relations*: At high density, the single-particle spectra are significantly modified from their noninteracting forms due to effects of strong interactions. Interacting matter features smaller effective baryon masses and energy shifts relative to non-interacting matter.
- (3) *Correlations*: Repulsive particle-hole interactions and Coulomb interactions generally result in a screened dielectric response and also lead to collective excitations in matter.

These effects may be calculated using the Random Phase Approximation (RPA), in which ring diagrams are summed to all orders. Model calculations (Sawyer 1975,1989; Iwamoto & Pethick 1982; Horowitz & Wehrberger 1991a,b; 1992, Raffelt & Seckel 1995, Sigl 1995, Reddy et al. 1997, Prakash & Reddy 1997, Burrows & Sawyer 1998a,b) indicate that at high density the neutrino cross sections are suppressed relative to the case in which these effects are ignored. In addition, these correlations enhance the average energy transfer in neutrino-nucleon collisions. Improvements in determining the many-body dynamic form factor and assessing the role of particle-particle interactions in dense matter at finite temperature are necessary before the full effects of many-body correlations may be ascertained.

(4) *Axial charge renormalization*: In dense matter, the axial charge of the baryons is renormalized (Wilkinson 1973, Rho 1974, Brown & Rho 1991), which alters the neutrino-baryon couplings from their vacuum values. Since the axial contribution to the scattering and absorption reactions is typically three times larger than the vector contributions, small changes in the axial vector coupling constants significantly affect the cross sections.

(5) *Multi-Pair excitations*: Neutrinos can also excite many-particle states in an interacting system, inverse bremsstrahlung being an example of a two-particle excitation (Hannestad & Raffelt 1998). These excitations provide an efficient means of transferring energy between the neutrinos and baryons which are potentially significant in low-density matter. However, multigroup neutrino transport will be needed to fully include this affect. In addition, such calculations require source terms for neutrino processes such as bremsstrahlung and neutrino pair production. The latter process has been accurately treated by Pons, Miralles, & Ibañez (1998).

The relative importance of the various effects described above on neutrino transport is only beginning to be studied systematically. As a first step, we will focus on effects due to modifications (1) and (2) above, since RPL have shown how to calculate them consistently with the underlying EOS. Work on the other modifications listed above is currently in progress and will be incorporated in a future publication. In what follows, we recapitulate some of the essential results for the evaluation of the neutrino mean free paths and diffusion constants.

The scattering and absorption reactions that contribute to the neutrino opacity are

$$\nu_e + B \rightarrow e^- + B', \quad \bar{\nu}_e + B \rightarrow e^+ + B', \quad (57)$$

$$\nu_X + B \rightarrow \nu_X + B', \quad \nu_X + e^- \rightarrow \nu_X + e^-, \quad (58)$$

where the scattering reactions are common to all neutrino species and the dominant source of opacity for the electron neutrinos is due to the charged reaction. The total cross section per unit volume for the scattering reaction $\nu + B \rightarrow \nu' + B'$ and absorption reaction

$\nu + B \rightarrow e^- + B'$ are given by

$$\frac{\sigma(E)}{V} = \frac{G_F^2}{2\pi^2 E^2} \int_{-\infty}^E dq_0 \frac{(1 - f(E'))}{1 - \exp(-z)} \int_{|q_0|}^{2E - q_0} dq q q_\mu^2 [AR_1 + R_2 + BR_3]. \quad (59)$$

where E and E' are incoming and outgoing lepton energies, and $q_\mu = (q_0, \vec{q})$ is the four momentum transfer to the baryons so that $q_\mu^2 = 2EE'(\cos\theta - 1)$, where θ is the angle between the incoming and outgoing lepton. The factor $(1 - \exp(-z))$ arises due to the principle of detailed balance, and $z = (q_0 + \mu_B - \mu_{B'})/T$. The response functions R_1 , R_2 , and R_3 are functions of the energy and momentum transfers $q_0 = E - E'$ and $\vec{q} = \vec{k} - \vec{k}'$, and strongly depend on the properties of matter, such as the individual particle degeneracies and in-medium modifications to the baryon propagators. The density and temperature dependent baryon effective masses and chemical potentials required for their evaluation are obtained directly from the EOS. Explicitly, the response functions are written in terms of the neutrino baryon coupling constants \mathcal{V} and \mathcal{A} , and the polarization functions

$$R_1 = (\mathcal{V}^2 + \mathcal{A}^2) [\text{Im } \Pi_L^R(q_0, q) + \text{Im } \Pi_T^R(q_0, q)] \quad (60)$$

$$R_2 = (\mathcal{V}^2 + \mathcal{A}^2) \text{Im } \Pi_T^R(q_0, q) - \mathcal{A}^2 \text{Im } \Pi_A^R(q_0, q) \quad (61)$$

$$R_3 = 2\mathcal{V}\mathcal{A} \text{Im } \Pi_{VA}^R(q_0, q). \quad (62)$$

In the case of absorption $\mathcal{V} = Cg_V$ and $\mathcal{A} = Cg_A$, where C is the Cabibbo factor, g_V and g_A are the vector and axial-vector couplings. For scattering reactions $\mathcal{V} = g_V/2$ and $\mathcal{A} = g_A/2$, respectively. Numerical values are taken from Tables I and II of RPL. The imaginary part of the various polarization functions Π may be found in (Horowitz & Wehrberger 1991, 1992; RPL 1998). Comparing with equation (20) we identify

$$R_s^{out} = 4G_F^2 \frac{(\cos\theta - 1)}{1 - e^{-z}} [AR_1 + R_2 + BR_3] \quad (63)$$

$$\frac{1}{\lambda_a} = \frac{G_F^2}{\pi^2} \int_0^\infty dE_e E_e^2 [1 - f_{eq}(E_e)] \int_{-1}^{+1} d\cos\theta \frac{(\cos\theta - 1)}{1 - e^{-z}} [AR_1 + R_2 + BR_3] \quad (64)$$

Note that the above formalism accounts for the effects arising due to matter degeneracy and in-medium modifications in the baryon dispersion relations exactly. As stated earlier, ignoring the effects due to correlations, the total scattering kernel R_s^{out} is simply the incoherent sum over all possible scattering process. Similarly, the absorption mean free path λ_a is the sum over all possible absorption reactions.

Under degenerate conditions even modest changes to the composition significantly alter the neutrino scattering and absorption mean free paths. In Figure 6, the neutrino scattering and absorption cross sections are shown for models GM3np and GM3npH relevant to the deleptonization and cooling epochs. The top panels show the scattering cross sections

common to all neutrino species in neutrino free matter. The scattering cross section per unit volume for thermal neutrinos ($E_\nu = \pi T$) is shown in the left panel for various temperatures. To study the influence of hyperons, the ratio of the σ_{npH}/σ_{np} is shown in the right panels. The presence of hyperons significantly increase the scattering cross sections, by a factor $\sim (2 - 3)$. Similar results for the absorption cross sections are shown in the lower panels for $Y_L = 0.4$. Again we notice a significant enhancement (right panel) when hyperons appear, the factor here could be as large as 5.

During the deleptonization stage, lepton number transport is sensitive to charged current reactions which dominate scattering reactions. At zero temperature, charged current reactions $\nu + n \leftrightarrow e + p$ depend sensitively on the proton fraction Y_p (Lattimer et al. 1991). Kinematic restrictions require Y_p to be larger than 11 – 14% (direct Urca threshold). At early times, a finite neutrino chemical potential favors a large Y_p throughout the star, which enables these reactions to proceed without any hindrance. Toward the late stages, however, Y_p decreases with decreasing μ_ν and charged current reactions may be naively expected to become inoperative. The threshold density for the charged current reaction when $\mu_\nu = 0$ and $T = 0$ depends sensitively on the density dependence of the nuclear symmetry energy. In field-theoretical models, in which the symmetry energy is largely given by contributions due to ρ -meson exchange, the critical density is typically $n_B = 2 \sim 3n_0$. However, finite temperatures favor larger Y_p 's and increase the average neutrino energy enabling the charged current reactions to proceed even below these densities. Figure 7 shows that this is the case even at relatively low temperatures ($T \sim 3 - 5$) MeV for a baryon density $n_B = 0.15 \text{ fm}^{-3}$. The sharp rise with temperature, which occurs even for $Y_\nu = 0$, clearly indicates that this reaction dominates the ν_e opacity even during the late deleptonization era. Thus, charged current reactions cannot be simply turned off when the neutrino chemical potential becomes small enough as was done in prior PNS simulations (BL).

The EOS and neutrino mean free paths are intimately related, which is best illustrated by comparing the results shown in Figure 6 with those shown in Figure 8. Composition and the baryon effective masses influence both the neutrino mean free paths and the matter's specific heat. Hyperons decrease the neutrino mean free paths at constant temperature (Figure 6). This trend is reversed at constant entropy due to the significantly lower temperatures favored in npH matter. Similar effects are apparent when we compare np models with different baryon effective masses. At a constant temperature, the larger effective mass in model GM3np favors larger cross sections, while at constant entropy this trend is again reversed due to the lower temperatures favored by the larger specific heat.

The diffusion coefficients are calculated using equation (32) with the cross sections discussed above. Earlier works (BL & KJ) made simplifying assumptions to define the diffusion coefficients including the use of interpolation to bridge the degenerate and

nondegenerate limits. But in partially degenerate matter, effects due to Fermi motion and Pauli blocking are substantial. The effects of density-dependent baryon effective masses, which are significant, were also ignored. In this work, we numerically integrate equation (32) over the neutrino energies by employing the exact cross sections. The diffusion coefficients D_2 , D_3 , and D_4 are functions of n_B , T , and Y_{ν_e} .

5. RESULTS AND DISCUSSION

5.1. Baseline Model

We have performed simulations for several dense matter models, initial conditions and baryonic masses. To begin, we describe in detail the general features of a reference model, corresponding to the dense matter EOS containing nucleons and leptons (model GM3np), and for a baryon mass $M_B = 1.6 M_\odot$. We shall initially concentrate on the temporal evolution of the various thermodynamic quantities, such as s , T , n_B , Y_e , Y_ν and μ_ν inside the PNS (see Figure 9). Our overall results are qualitatively similar to those obtained in earlier works (BL; KJ), but some interesting differences exist nevertheless.

The initial entropy and Y_L profiles were taken from the profiles obtained in detailed core collapse calculations of an $M_B = 1.08 M_\odot$ star (Wilson & Mayle 1989) within a hundredth of a second of core bounce. For larger mass PNSs, the s and Y_L profiles were scaled in terms of the relative enclosed baryon mass. At early times $Y_L \sim 0.36$ and $s \sim 1$ in the central regions, while the shocked outer mantle which begins at about $0.5 M_\odot$ (for the $1.08 M_\odot$ star) is at high entropy ($s \geq 8$) and contains smaller lepton fractions. The outermost regions, which contains subnuclear density matter, and tends to nearly symmetric matter at low density, hence, it contains a large positive gradient in electron concentration. By scaling the results for $1.08 M_\odot$ for larger masses, we attempted to simulate the profiles expected for larger collapsing stars. The masses of both the inner core with roughly constant s and Y_L and the shocked, relatively lepton-poor outer mantle should increase with total mass.

The evolution of the $1.6 M_\odot$ star proceeds as follows. The steep neutrino chemical potential gradients drive a radially outward flow of electron neutrinos, causing deleptonization. The most rapid deleptonization occurs in the low-density outer mantle, which collapses during the first few tenths of a second due to substantial pressure loss from neutrino emission. Note from Figure 9 that compression of the outer half of the star leads to a significant temperature increase. The deleptonization of the central regions takes much longer, tens of seconds in this example. The central regions, as they deleptonize, are also heated due to neutrino transport (Joule heating). Eventually, after about 15 seconds, the central heating is overwhelmed by neutrino cooling and the central temperature begins a steady decrease. This star took about 50 seconds to cool to below 5 MeV temperatures in

the central regions. At these low temperatures, the neutrino mean free path has increased to values approaching that of the stellar radius and the star became transparent to neutrinos. Beyond this time, diffusion is no longer a valid approximation to the transport equations; however, the neutrino luminosities are very low (see below) and perhaps even undetectable.

Qualitatively, the simulations of BL are similar: the central entropy rises from $s = 1$ to the peak value of about $s = 2$ in about 15 seconds, and neutrino transparency occurs after about 50 s. However, one significant difference is that at the beginning of the central cooling epoch, when the central temperature reaches a maximum, there are still substantial numbers of trapped neutrinos present ($\mu_\nu \gg T$). Consequently, in our simulations the deleptonization continues through most of the cooling epoch as well. We attribute this difference to differences in the treatment of the nuclear absorption processes. In the calculations of BL, the absorption cross section does not contain any explicit temperature dependence and, further, is assumed to vanish when Y_e fell below a critical value of about $1/9$. The value $1/9$ corresponds to the critical proton fraction below which the direct Urca process is prohibited at zero temperature (Lattimer et al. 1991), in the absence of muons (both BL and this paper neglect muons). However, as shown in Figure 7, the absorption cross section does not behave as a step function as long as the temperature is above a few MeV. In addition, BL used a symmetry energy with almost no density dependence, with the result that $\mu_n - \mu_p$, and consequently the equilibrium value of the proton fraction, decreased to the critical value relatively early in the deleptonization. Hence, in our calculation, absorption contributes to the opacities for a much longer time than in BL, so that the decrease of μ_ν in the central regions is suppressed.

Despite the differences in the evolution of μ_ν , the long-timescale cooling is dominated by mu- and tau-neutrinos. The upper panels of Figure 10 shows neutrino mean free paths for an average energy, $\langle E_\nu \rangle = \mu_\nu + \pi T$, for four times during the evolution. The mu- and tau-neutrino mean free paths are significantly larger than those for electron neutrinos. Note that the mean free paths in the central regions initially shrink as the star becomes denser and hotter, but by 15 s they begin to increase due to the decreasing temperature. It is also clear that the mu- and tau-neutrino mean free paths are more sensitive to the temperature than they are to the density, and their temperature dependence is greater than for electron neutrinos. The profiles for λ_{ν_μ} are nearly mirror images of the temperature profiles for each time. Despite the fact that $\lambda_{\nu_\mu}/\lambda_{\nu_e} > 1000$ at early times in the core, there are so few mu- and tau-neutrinos relative to electron-neutrinos that the transport is dominated by ν_e s. However, by 15 s, $\lambda_{\nu_\mu}/\lambda_{\nu_e} < 100$ and the thermal evolution becomes dominated by mu- and tau-neutrinos.

5.2. Dependence Upon Initial Conditions

A major uncertainty exists in the specifications of the initial entropy and Y_L profiles. These are not accurately known because they depend on the details of the EOS and weak interaction physics employed both during the late evolution of the precollapse stars and the collapse of the core (Wilson & Mayle 1989, Swesty, Lattimer, & Myra 1994, Mezzacappa & Bruenn 1993). Ever since the work of Bethe et al. (1979), it has been realized that the inner core of the PNS should have canonical values of $s \approx 1$ and $Y_L \approx 0.38$. Depending upon electron capture and beta decay rates and upon the symmetry energy, the entropy could be 50% larger or smaller and Y_L could vary by ± 0.03 . In addition, the s and Y_L profiles in the shocked matter at enclosed baryon masses greater than $0.6 M_\odot$ (in the $M_B = 1.6 M_\odot$ star) depend upon the strength of the outgoing shock and also, perhaps, upon convective instabilities.

We performed several simulations of the $M_B = 1.6 M_\odot$ GM3np star in order to study the sensitivity of the early evolution to the s and Y_L profiles at $t = 0$. The spatial variation of various physical quantities for $t = 0, 1, 5$, and 15 seconds for models with lower (higher) initial central entropies are shown as dashed curves in Figure 11 (Figure 12), compared to the baseline model, which are displayed as solid lines. These variations do not produce dramatic effects, but the differences in thermodynamic quantities, although damped, persist to late times. Lowering the initial central entropy results in a higher value for μ_ν , since the central density is increased because of the lessening of thermal pressure. However, by 15 s, the values of μ_ν actually fall below that of the baseline simulation, because the evolution is more rapid due to the lower temperatures and relatively longer mean free paths. Exactly the opposite behavior occurs when the initial central entropy is increased.

In Figure 13, we show the effects of increasing the lepton concentrations throughout the star; the central value of Y_L is increased from 0.36 to 0.40. Since there are now more leptons to lose, the simulation results in more heating, which contributes toward longer evolution time scales. However, the effects are far smaller than in the case in which the core entropies were changed.

We also considered variations of the entropy in the shocked mantle material; this case is shown as dotted lines in Figure 12. Note that although the entropy is larger at all masses in the initial model, the temperatures are uniformly lower. This counterintuitive situation results from the additional expansion of the outer stellar layers: the density at all masses are also smaller in this case. Nevertheless, due to the rapid and extreme compression of the outer layers, these variations are completely swamped and there is virtually no difference between this and the baseline cases visible after a second. The same is true of simulations with variations in the lepton concentration in the shocked mantle material, which we do not display. Variations of entropy and lepton fraction in these outer regions manifest themselves

as short-term (a few tenths of a second) transients in the neutrino luminosities, which are discussed in §5.5. We can conclude that only variations of the initial conditions in the central regions of the PNS are relatively important in the long-term evolution.

A useful summary of the effects of variations in initial conditions is contained in Figure 14, which displays the total neutrino luminosity as a function of time. Varying the central values of the entropy produce persistent differences in the luminosity. This is due to two factors: first, the initial binding energies of lower entropy models is larger, so the integrated luminosities must be smaller, and second, the evolution time scales of the lower entropy models must be more rapid, due to the lower temperatures and longer neutrino mean free paths. Similar behavior is produced by varying the central values of Y_L : higher values of Y_L reduce the initial binding energy and also lead to more entropy generation, higher temperatures, and longer diffusion times. Altering entropy and lepton profiles in the shocked mantle has little effect except in the first few tenths of a second.

The observed variations in luminosity and average energy due to uncertainties in initial conditions are relatively small, but nevertheless will contribute to uncertainties in distinguishing EOS and compositional variations from an observed neutrino signal.

5.3. EOS Dependence

Equations of state differ in many respects at high densities. Most significant for the PNS are variations in compressibilities, symmetry energies, specific heats, and compositions. To study these effects, we consider three relativistic field-theoretical models with different high density properties. For two of these models, we also consider the possible presence of hyperons. These models do not necessarily encompass the entire range of possible behaviors. For example, we could have considered models with more extreme density dependences of the baryon effective masses, which are important in the determination of the specific heats, or the symmetry energy, which plays a role in determining the composition and the neutron star radius. However, the results of such variations may be gauged from the results we present here.

The left panels of Figure 15 and Figure 16 compare the evolutions of a PNS of an $M_B = 1.6 M_\odot$ star for the parameter sets GM3 and GM1 for nucleons-only matter for the $1.6 M_\odot$ baryon mass star. GM1 is a stiffer EOS, and it has a lower value of the baryon effective mass M^* . Therefore, the densities in the GM3np models are uniformly greater than in the GM1np models. The GM3np temperatures are also greater; the higher densities more than compensate for the greater specific heat compared to GM1np. As a result of the higher temperatures and densities, the neutrinos are more tightly trapped, there is more entropy generation, and the evolution times are longer in the GM3np models. When

hyperons are included, as shown in the right panels of Figure 15 and Figure 16, the GM1 and GM3 models display the same relative trends.

Comparing models with and without hyperons, *i.e.*, the right and left panels of Figure 15 and Figure 16, the initial models ($t = 0$ s) with hyperons show a small amount of softening. The central density of the hyperon stars becomes progressively larger than that of the purely nucleon stars, largely because of the appearance of thermal hyperons. The central densities of the hyperon stars remains larger even at late times when the remnant is cooling because hyperons are present. Little difference in the temperature evolution of these cases is apparent even after 20 s. Nevertheless, the evolution time scale of hyperon stars is slightly larger than for purely nucleon stars, due to the smaller mean free paths of hyperonic matter (see Figure 10). An interesting feature is the appearance of a trough in Y_e and Y_ν near $0.75 M_\odot$ at $t = 0.5$ s. This feature is a short lived transient, because it does not appear in Figure 13 which shows Y_L for $t=1$ s.

The major effects on the temporal evolution are more easily seen by examining Figure 17, which shows the time development of important physical variables at the star’s center. It is clear that deleptonization continues during the subsequent cooling epoch. One should also note the plateau in the decay of Y_ν and μ_ν in the case of GM3np and GM1np. This is due to the density sensitivity of the neutrino mean free paths. With hyperons, larger central densities and higher electron neutrino energies are reached. This increases the neutrino opacity, temporarily reducing the loss of neutrinos from the stellar core.

Figure 18 shows the luminosities and the average neutrino energies as a function of time for the different EOS models, and for the baryon masses $M_B = 1.6M_\odot$ and $M_B = 1.8M_\odot$. The luminosities are virtually identical until about 10 s, at which point the luminosity for models with a stiffer high density EOS decrease more rapidly. Contrasting the models with and without hyperons, we find a similar trend, with the hyperon models being able to sustain a higher luminosity at late times. The average energy of the emitted neutrinos are more sensitive to the EOS; once again a clear trend emerges in which models with a stiffer high-density EOS favor lower average energies. The average energy for models with hyperons is about 10-15% larger than those observed in matter containing only nucleons. These contrasting features are accentuated at late times and with increasing mass.

We emphasize that for the mass ($1.6 M_\odot$) and coupling constants chosen for this comparison relatively few hyperons are present at early times (see left panel of Figure 19). In fact, the maximum concentration of hyperons at $t = 0$ is about 0.01%. However, as the density and temperature in the star is raised during deleptonization, the number and effect of hyperons becomes greater. Hyperons do not appear only at the star’s center; the large temperatures in the mantle around $1 M_\odot$ result in a higher concentration of hyperons there than at the center from 0.25 s to 2 s. At late times, the central density of the npH star is nearly 20% larger than the np star and the concentration of hyperons at the star’s center is

about 13%. For the mass ($1.8 M_{\odot}$), a significantly larger number of hyperons are present as can be seen from the results shown in the right panel of Figure 19. The interesting feature to note is that until about 15 s, the hyperons fractions are quite small, indicating that deleptonization in the inner core occurs very slowly. This is one of the reasons why we see very small changes in the observed luminosities between np and npH models at early times. In addition, feedbacks between the EOS and the opacities tend to reduce the differences.

5.4. Mass Dependence

We considered the effect of varying the initial mass of the PNS. For this study we employed the GM3 parameterization, and considered both np and npH matter. The actual baryon masses used in the simulations are listed in Table 3. The results displayed in Figures 18, 20, and 21 indicate that the most significant effect of increasing the initial mass is to increase the overall time scales of evolution, and to increase both the total and average energies released. The central heating also becomes more significant as one increases the remnant mass. Although the central entropy shows very little increase with increasing mass, the higher density of larger mass models translates into significant increases in central temperature. The combination of higher densities and temperatures lengthens the time constants associated with heating, cooling, and deleptonization. This naturally results in a longer duration of the plateau stage in the evolutions of Y_{ν} and μ_{ν} for np models. Note that these plateaus do not appear for npH matter for any mass. In spite of the larger time scales, the larger energy release, and increased temperatures larger mass models lead to larger luminosities at all times.

5.5. Metastability

The $M_B = 1.8M_{\odot}$ baryon mass star containing hyperons is metastable. After more than 100 s, this star will collapse to a black hole since the maximum baryon mass of the cold, catalyzed GM3npH EOS is $1.75 M_{\odot}$. The possibility of metastability has been suggested in the context of SN 1987A, for which no neutron star remnant has been observed (Bethe & Brown 1995, Prakash, Cooke, & Lattimer 1995, Ellis, Lattimer, & Prakash 1996, Prakash et al. 1997). The lack of a neutron star in this object seems peculiar, because a neutron star rotating with the frequency of the Crab pulsar and with a magnetic field only a fraction of the Crab’s field would be contributing noticeably to the light curve of the expanding gaseous remnant of SN 1987A. This is not observed. Although one cannot yet rule out the existence of a neutron star on the basis of Eddington-limit accretion, because the effective opacity may be due to iron instead of hydrogen and therefore be much greater, a black hole remnant seems a possibility. This hypothesis can be reconciled with the neutrino emission

observed from SN 1987A if the PNS was metastable because of the existence of hyperons or a kaon condensate in cold, catalyzed dense matter.

For this reason, we further explored the case of a metastable PNS for the GM3 parameterization. Figure 22 shows the time development of the central baryon density (top panel) and also the time to the collapse instability as a function of baryon mass (bottom panel). The larger the mass, the shorter the time to instability, since the PNS doesn't have to evolve in lepton number as much. Above $2.005 M_{\odot}$, the metastability disappears because the GM3npH initial model with the lepton and entropy profiles we chose is already unstable. Below about $1.73 M_{\odot}$, there is no metastability, since this is the maximum mass of the cold, catalyzed npH star for GM3. These values are listed in Table 2, which contains corresponding, but larger, values for the case of GM1. The signature of neutrino emission from a metastable PNS should be identifiable and it is discussed in §5.7.

Figure 23 shows the behavior of the quantity GM_G/Rc^2 as functions of both the radius and the enclosed baryon mass for a GM3npH model with $M_B = 1.88 M_{\odot}$. The time to instability for this model is slightly more than 45 s. Although the actual collapse to form a black hole is dynamic, and in any event could never be seen from the outside, one could estimate that the event horizon is likely to form where the redshift is largest. With time, it appears that this point moves outwards in the star, so that the event horizon can be expected to form relatively close to the star's physical surface and, therefore, outside the star's neutrinosphere.

5.6. Convective Instabilities

The possibility of convection in PNS has been discussed by a number of authors (Burrows & Fryxell 1993, Herant et al. 1994, Keil, Janka, & Müller 1996, Mezzacappa et al. 1998). The decreasing entropy gradient in the star's exterior is obviously convectively unstable, and this gradient works its way into the interior on the deleptonization time scale. However, the complete determination of convective instability also requires knowledge of the lepton gradients. Explicitly, we consider the Ledoux criterion for convectively unstable regions: the condition is $C_L(r) > 0$, where

$$C_L(r) = -\frac{1}{\left(\frac{\partial P}{\partial n_B}\right)_{s,Y_L}} \left[\left(\frac{\partial P}{\partial s}\right)_{n_B,Y_L} \frac{ds}{dr} + \left(\frac{\partial P}{\partial Y_L}\right)_{s,n_B} \frac{dY_L}{dr} \right]. \quad (65)$$

We show in Figure 24 the unstable regions of a PNS for the GM3np and GM3npH models for $M_B = 1.6 M_{\odot}$ as shaded regions. Generally, the outermost few tenths of a solar mass is initially unstable. After a few seconds, the instability moves inwards, reaching the center after 10–15 seconds. We do not allow for convection in our simulations, so the result that

after a few seconds the exterior of the star becomes stable against convection is unreliable. In fact, the calculations of Keil, Janka, & Müller (1996) show that the convection proceeds similarly to what our models show, but that the exterior remains convectively unstable throughout the evolution. Their time scales are, however, much shorter in comparison to our findings. The influence of convection upon the luminosities and average neutrino energies has been shown by prior authors (Burrows & Lattimer 1988) to be relatively significant, and we will consider this effect in the next generation of our calculations.

5.7. Signals in Terrestrial Detectors

Knowledge of the neutrino luminosities and energies permit the signal from a supernova to be calculated. To be specific, we will present results in a way that makes comparison to the signal observed from SN 1987A (Bionta et al. 1987, Hirata et al. 1987) transparent. We assume two fiducial detectors, KII and IMB, whose masses, thresholds and efficiencies are taken to be the same as in Lattimer & Yahil (1989). We focus on the antineutrino signal, assuming that the antineutrino luminosity $L_{\bar{\nu}}$ is 1/6 of the total.

We assume a pure water detector for which the cross section of antineutrinos absorbed onto protons is $\sigma(E_{\nu}) = \sigma_0 E_{\nu}^2$ where E_{ν} is the antielectron neutrino energy in MeV and $\sigma_0 = 9.3 \cdot 10^{-44}$ cm². There are $n_p = 6.7 \cdot 10^{28}$ free protons per kiloton of water. We take the distance to SN 1987A to be $D = 50$ kpc. Assuming that the neutrinos leaving the protoneutron star have a Fermi-Dirac spectrum with zero chemical potential, the count rate is

$$\frac{dN}{dt} = \left(\frac{R_{\nu}^{\infty}}{D}\right)^2 \frac{c\sigma_0 n_p}{8\pi(\hbar c)^3} \mathcal{M} \int_{E_{th}}^{\infty} E_{\nu}^4 f(E_{\nu}, T_{\nu}^{\infty}) W(E_{\nu}) dE_{\nu}, \quad (66)$$

where E_{th} is the detector threshold, W is the detector efficiency and \mathcal{M} is the detector mass in kilotons. Also, $R_{\nu}^{\infty} = e^{-\phi_s} R_{\nu}$ and $T_{\nu}^{\infty} = e^{\phi_s} T_{\nu}$, where $e^{\phi_s} = \sqrt{1 - 2GM_G/R_{\nu}c^2}$ and M_G and R_{ν} are the gravitational mass of the neutron star and the radius of the neutrinosphere, respectively. Since the luminosity is calculated more precisely than the neutrinospheric radius and temperature, we rewrite this, substituting the antineutrino luminosity, as

$$\frac{dN}{dt} = \frac{\sigma_0 n_p}{4\pi D^2} \mathcal{M} \frac{G_4(E_{th}, e^{\phi_s} T_{\nu})}{F_3(0)} e^{\phi_s} T_{\nu} L_{\bar{\nu}}, \quad (67)$$

where $F_3(0) = 7\pi^4/120$ is an ordinary Fermi integral and $G_i(E_{th}, T)$ denotes a modified, truncated Fermi integral:

$$G_i(E_{th}, T) = \int_{E_{th}}^{\infty} dz z^i W(zT) (1 + e^z)^{-1}. \quad (68)$$

In Figure 25 we display the count rate and integrated counts for KII and IMB for the $M_B = 1.6$ and $1.8 M_{\odot}$ models for the various EOS cases studied. The results can be

easily interpreted in terms of the average energies illustrated in Figure 18. While the total luminosities remain essentially identical for all cases of a given mass up to about 20 seconds, the average energies show a systematic variation. The softer the underlying EOS, the larger the average energy, and this directly translates into higher count rates. The general trends, which are explainable by the more extreme temperature sensitivity of the IMB detector, are that more counts accumulate in KII than in IMB and the time over which a signal is observed is also larger for KII than for IMB.

The total variation among the EOS models in the accumulated counts after 40 seconds is about 10% for a given mass. The mean ratio of total counts between the $1.8 M_{\odot}$ and $1.6 M_{\odot}$ cases is about 1.5. Therefore, it seems that for a Galactic supernova observed in the near future, in which the expected number of counts will be substantially larger because of its proximity and larger detectors, that the protoneutron star mass could be measured to better than $0.05 M_{\odot}$ from the total number of counts observed. It also seems that the more subtle differences between EOS models will be observable only if the accumulations after about 20 seconds are large enough.

5.8. Comparison with Earlier Work

We turn now to a comparison of our results with the earlier works of BL and KJ on the early evolution of protoneutron stars containing only nucleonic matter. There are important differences arising due to the different input physics. In these earlier works the neutrino opacities were not calculated consistently with the dense matter EOS. Thus, it is possible to compare only some aspects of previous calculations with our own. These aspects include the luminosity evolution and the average neutrino energies, as well as the evolution of temperature and neutrino number in the interior.

BL and KJ both found that, for 1.4 – $1.6 M_{\odot}$ star, the *deleptonization* time, the time needed for the electron neutrino number Y_{ν_e} to vanish in the star’s center, was about 10 s (see Figure 8 in BL & Figure 5 in KJ). In addition, they both found that the central temperature reached a maximum at about the time at which the neutrino number vanished. In contrast, we generally find that these two time scales are not similar: while the time required for the central temperature to reach a maximum is of order 10 seconds, the deleptonization time is much longer, at least 30 seconds. We attribute the more rapid deleptonization in earlier works to inadequate treatments of the temperature dependence of the direct Urca process, the nuclear symmetry energy and the matter’s specific heat. In our models, the larger electron neutrino cross sections at high temperature and low neutrino numbers stem the flow of electron neutrino number.

Comparing the calculations of BL in more detail, we find that the total luminosity is

larger during the deleptonization era. After 20 seconds in BL, nearly 1/3 of the binding energy has yet to be radiated (see Figure 19 in BL), while in our calculations at the same time less than 10% remains. Burrows, Klein, & Gandhi (1992) have argued that the neutrino luminosity evolves as a power law at late times (t larger than a few seconds), while it decays exponentially in ours. As Prakash et al. (1995) demonstrated, an effective E^2 behavior of the neutrino cross sections should result in an exponential decrease of temperature and luminosity for the star.

Another apparent difference between the calculations of BL and ours concerns the average emitted neutrino energy: in our calculation this peaks at about 5 s, while in BL it steadily decreases with time (see Figure 20 in BL). This difference could be important for the questions of neutrino-assisted shocks and for nucleosynthesis. However, it should be borne in mind that we estimated the average energy by the relation $\langle E_\nu \rangle = 3T_\nu$, but this neglects possible effects of neutrino degeneracy and the fact that the emergent spectrum may not be Fermi-Dirac. It will be necessary to employ more accurate transport in the vicinity of the neutrinosphere before firm conclusions can be drawn.

We see more substantial differences from the calculations of KJ. During the first few seconds of the evolution, KJ find that the central density decreases (see Figure 10 in KJ). KJ attribute this decrease to the heating which occurs during deleptonization. Indeed, KJ find a large increase in central temperature during the first five seconds (see Figure 11 in KJ) which is much more rapid than in our calculations. The effects of rapid deleptonization and rapid temperature increase could be explained by a charged-current mean free path that is several times larger than in our calculation. On the other hand, the cooling time scales, which are controlled by neutral current processes, are rather similar to what we have found. This probably also accounts for the remarkable similarities between our and KJ’s total neutrino luminosities, despite very different deleptonization times.

A decrease in central density during the deleptonization epoch could happen if the thermal contributions to the pressure at 3–5 times the nuclear density were a significant part of the total. However, this would imply that the specific heat of the matter is radically different than what we find.

We can also compare our proton-neutron star evolutions to KJ for cases in which hyperons appear. In contrast to their calculations, we find only minor differences in the evolution of nucleons-only and hyperon-bearing models at early times. In fact, for most masses studied, the evolutions of luminosity in our calculations for the two cases are nearly identical for about 20 seconds. KJ find that large differences in the luminosity occur between np and npH cases as early as 2–4 seconds (see Figure 9 in KJ) in the evolution. They found a time to collapse in the metastable case of less than 20 seconds when the stellar mass was $0.02 M_\odot$ larger than the critical mass (see Table 2 in KJ). For the same mass difference, we find a time to collapse of more than 100 seconds. These differences no

doubt stem from the same effects that led to the large differences apparent between KJ’s and our nucleon models. Our relatively large deleptonization times prevent hyperons from flooding the interior until rather late times. This significantly increases the time spent in the metastable phase when the mass is only marginally above the maximum mass for cold, deleptonized matter (see Figure 22).

6. Summary and Outlook

In this paper, we presented calculations of protoneutron star evolutions which used neutrino opacities that were consistently determined from the underlying dense matter EOS. We explored the sensitivity of the results to the initial stellar model, the total mass, the underlying EOS, and the addition of hyperons. We find that the differences in predicted luminosities and emitted neutrino energies do not depend much upon the details of the initial models or the underlying high-density EOS for early times ($t < 20$ s), provided that opacities are calculated consistently with the EOS. The same holds true for models which allow for the presence of hyperons, except when the initial mass is significantly larger than the maximum mass for cold, catalyzed matter. Increasing the total mass tends to increase luminosities and average energies at all times. For times larger than about 10 seconds, and prior to the occurrence of neutrino transparency, the neutrino luminosities decay exponentially with a time constant that is sensitive to the high-density properties of matter. We also find the average emitted neutrino energy increases during the first 5 seconds of evolution, and then decreases nearly linearly with time. *Metastable stars, those with hyperons which are unstable to collapse upon deleptonization, have relatively long evolution times, which increase the nearer the mass is to the maximum mass supported by a cold, deleptonized star.*

There are several interesting and possibly important physical effects that remain to be investigated.

(1) In terms of input neutrino opacities, this work provides a baseline calculation in terms of which further improvements (Reddy et al. 1997, Prakash & Reddy 1997, Burrows & Sawyer 1998a;b, Hannestad & Raffelt 1998) such as the effects of many-body correlations, axial charge renormalization and multi-pair excitations may be assessed.

(2) While the diffusion approximation is valid for a significant portion of the star at early times, neutrino transport in the semi-transparent regions is better handled in a multigroup transport scheme. Better transport in the semi-transparent regions will play an important role in determining the average neutrino energies for the different neutrino species and their energy spectra.

(3) An adequate treatment of convection coupled with neutrino transport appears to be necessary based on the large regions we identified as being convectively unstable.

(4) Other softening components in dense matter might produce effects dissimilar to those we find when considering hyperons. For example, the appearance of a Bose condensate differs from the appearance of hyperons because the condensate does not contribute to the matter’s specific heat. In addition, the presence of a condensate could produce distinctive modifications to the neutrino opacities.

Results of calculations incorporating these improvements will be reported subsequently.

We gratefully acknowledge encouragement and suggestions from Adam Burrows. We thank Thomas Janka and Wolfgang Keil for sharing information concerning some of the initial models used in this work. This work was supported in part by the U.S. Department of Energy under grant numbers DOE/DE-FG02-88ER-40388 and DOE/DE-FG02-87ER-40317, and by the NASA grant NAG52863. J. Pons gratefully acknowledges research support from the Spanish DGICYT grant PB94-0973 and thanks J.M. Ibañez for useful discussions.

REFERENCES

- Bethe, G.E., & Brown, G.E. 1995, *ApJ*, 445, L129
- Bethe, G.E., Brown, G.E., Applegate., J., & Lattimer, J.M. 1979, *Nucl. Phys.*, B348, 345
- Bionta, R. M., et al., 1987, *Phys. Rev. Lett.*, 58, 1494
- Bowers, R. L., & Wilson, J. R. 1982, *ApJS*, 224 50, 115
- Brown, G.E., & Rho, M. 1991, *Phys. Rev. Lett.*, 66, 2720
- Bruenn, S., 1985, *ApJS*, 58, 771
- Burrows, A., 1988, *ApJ*, 334, 891
- , 1990, *Ann. Rev. Nucl. Sci.*, 40, 181
- Burrows, A., & Fryxell, B. 1993, *ApJ*, 418, L33
- Burrows, A., Hayes, J., & Fryxell, B. A. 1995, *ApJ*, 450, 830
- Burrows, A., & Goshy, J. 1993, *ApJ*, 416, L75
- Burrows, A., Klein, D., & Gandhi, R. 1992, *Phys. Rev. D*, 45, 3361
- Burrows, A., & Lattimer, J. M. 1986, *ApJ*, 307, 178
- Burrows, A., & Lattimer, J. M. 1988, *Phys. Rep.*, 163, 51
- Burrows, A., & Sawyer, R. F. 1998a, *Phys. Rev. C*, In press
- Burrows, A., & Sawyer, R. F. 1998b, *Phys. Rev. Lett.*, (submitted)
- Ellis, P.J., Lattimer, J.M., & Prakash, M. 1996, *Comments on Nucl. & Part. Phys.*, 22, 63
- Glendenning, N.K., & Moszkowski, S. 1991, *Phys. Rev. Lett.*, 67, 2414
- Hannestad, S., & Raffelt, G. 1998, *ApJ* (in press)
- Herant, M., Benz, W., Hicks, J., Fryer, C. & Colgate, S.A. 1994, *ApJ*, 435, 339
- Hirata, K., et al., 1987, *Phys. Rev. Lett.*, 58, 1490
- Horowitz, C.J., & Wehrberger, K. 1991a, *Nucl. Phys.*, A531, 665
- , 1991b, *Phys. Rev. Lett.*, 66, 272
- , 1992, *Phys. Lett. B*, 226, 236
- Iwamoto, N., & Pethick, C. J. 1982 *Phys. Rev. D*, 25, 313
- Janka, H. T., Keil, W., Raffelt, G., & Seckl, D. 1996, *Phys. Rev. Lett.*, 76, 2621
- Keil, W. 1994, *Prog. Part. Nucl. Phys.*, 32, 105
- Keil, W., & Janka, H.T. 1995, *A&A*, 296, 145
- Keil, W., Janka, H.T., & Müller, E. 1995, *ApJ*, 473, L111
- Knorren, R., Prakash, M., & Ellis, P. J. 1995, *Phys. Rev. C*, 52, 3470
- Lattimer, J.M., Pethick, C.J., Prakash, M., & Haensel, P. 1991, *Phys. Rev. Lett.*, 66, 2701
- Lattimer, J.M., & Yahill, A. 1989, *ApJ*, 340, 426
- Levermore, C. D., & Pomraning, G. C. 1981, *ApJ*, 248, 321
- Lindquist, R.W. 1966, *Ann. Phys.*, 37, 478
- Mayle, R., Wilson, J.R., & Schramm, D.N. 1987, *ApJ*, 318, 288
- Mezzacappa, A., & Bruenn, S.W. 1993, *ApJ*, 405, 637

- Mezzacappa, A., Calder, A. C., Bruenn, S. W., Blondin, J. M., Guidry, M. W., Strayer, M. R., & Umar, A. S. 1998, *ApJ*, 495, 911
- Pons, J.A., Miralles, J.A. & Ibañez, J.-M. 1998, *A&AS*, 129, 343
- Prakash, M., Bombaci, I., Manju Prakash, Ellis, P.J., Lattimer, J.M., & Knorren, R. 1997, *Phys. Rep.*, 280, 1
- Prakash, M., Cooke, J., & Lattimer, J.M. 1995, *Phys. Rev. D*, 52, 661
- Prakash, M., & Reddy, S. 1997, in *Nuclear Astrophysics, in Proceedings of the International Workshop XXVI on Gross Properties of Nuclei and Nuclear Excitations*, Hirschegg, Austria, Jan 11-17, ed M. Buballa, W. Nörenberg, J. Wambach, & A. Wirzba, (GSI: Darmstadt), pp. 187-200
- Raffelt, G. & Seckel, D. 1995, *Phys. Rev. D*, 52, 1780
- Reddy, S., Pons, J., Prakash, M., & Lattimer, J.M. 1997, in *Second Oak Ridge Symposium on Atomic and Nuclear Astrophysics*, Oak Ridge, Tennessee, Dec 2-6, 1997
- Reddy, S., & Prakash, M. 1997, *ApJ*, 423, 689
- Reddy, S., Prakash, M., & Lattimer, J. M. 1998, *Phys. Rev. D*, 58, 013009
- Rho, M. 1974, *Nucl. Phys. A*, 231, 493
- Sawyer, R. F. 1975, *Phys. Rev. D*, 11, 2740
- , 1989, *Phys. Rev. C*, 40, 865
- , 1995, *Phys. Rev. Lett.*, 75, 2260
- Serot, B.D., & Walecka, J.D. 1986, in *Advances in Nuclear Physics*, Vol 16, ed. J.W. Negele & E. Vogt, (New York: Plenum), 1
- Sigl, G. 1996, *Phys. Rev. Lett.*, 76, 2625.
- Suzuki, H. 1989, Ph.D Thesis, University of Tokyo
- Suzuki, H., & Sato, K. 1992, in *The Structure and Evolution of Neutron Stars*, ed. D. Pines, R. Tamagaki, & S. Tsuruta, (New York: Addison-Wesley), 276
- Swesty, F.D., Lattimer, J.M., & Myra, E. 1994, *ApJ*, 425, 195
- Thorne, K. S. 1981, *MNRAS* 194, 439
- Wilkinson, D.H. 1973, *Phys. Rev. C*, 7, 930
- Wilson, J.R., 1985, in *Numerical Astrophysics*, eds. J. Centrella, J. LeBlanc, and R. Bowers (Jones and Bartlett, Boston) p. 422
- Wilson, J.R., & Mayle, R.W., 1989, in *The Nuclear Equation of State*, Part A, ed. W. Greiner and H. Stöcker (New York: Plenum), 731
- Woosely, S.E., Wilson, J.R., Mathews, G.J., Hoffman, R.D., & Meyer, B.S. 1994, *ApJ*, 433, 229

TABLE 1

NUCLEON-MESON COUPLING CONSTANTS

Model	K_0	a_{sym}	M^*/M	g_σ/m_σ	g_ω/m_ω	g_ρ/m_ρ	b	c
GM1	300	32.5	0.70	3.434	2.674	2.100	0.002950	-0.00107
GM3	240	32.5	0.78	3.151	2.195	2.189	0.008659	-0.002421
GM4	240	27.5	0.78	3.151	2.195	1.862	0.008659	-0.002421

NOTE.– Coupling constants for the GM (Glendenning & Moszkowski 1991) models which are calibrated at the nuclear equilibrium density $n_0 = 0.153 \text{ fm}^{-3}$ to give an energy per particle of symmetric nuclear matter of -16.3 MeV . The compression modulus K_0 , symmetry energy a_{sym} and Dirac effective mass M^* for the different models are also listed.

TABLE 2

MAXIMUM GRAVITATIONAL(BARYONIC) MASSES

Model	$Y_L = 0.4 (s = 1)$	$Y_\nu = 0 (s = 2)$	$Y_\nu = 0 (s = 0)$
GM1np	2.278(2.609)	2.367(2.748)	2.346(2.805)
GM3np	1.946(2.181)	2.044(2.328)	2.005(2.345)
GM1npH	2.024(2.259)	1.793(1.991)	1.776(2.020)
GM3npH	1.768(1.944)	1.573(1.726)	1.544(1.732)

NOTE.– Symbols are Y_L : the total lepton fraction, Y_ν : electron neutrino fraction, and s : the total entropy per baryon (in units of Boltzmann’s constant). Model designations are as in Table 1 with np referring to nucleons-only matter and npH referring to matter including hyperons.

TABLE 3

BARYONIC MASSES OF PNS EVOLUTION MODELS

Mass Label	Actual Mass (M_\odot)	Mass Label	Actual Mass (M_\odot)
1.08	1.0852	1.84	1.8434
1.4	1.4038	1.88	1.8843
1.6	1.6125	1.90	1.9038
1.8	1.7981	1.94	1.9413
1.81	1.8162	1.98	1.9863

FIGURE CAPTIONS

FIG. 1.– Relative concentrations in lepton-poor (left panels) and lepton-rich (right panels) matter at finite entropy as a function of baryon density n_B (n_0 is the nuclear equilibrium density). Top panels show results in nucleons-only matter. The bottom panels are for matter including hyperons.

FIG. 2.– Total pressure including contributions from leptons in lepton-poor (left panels) and lepton-rich (right panels) matter at finite entropy as a function of baryon density n_B (n_0 is the nuclear equilibrium density). The symbol np refers to matter with nucleons-only and npH to matter including hyperons.

FIG. 3.– Temperatures attained in lepton-poor (left panels) and lepton-rich (right panels) matter at finite entropy as a function of baryon density n_B (n_0 is the nuclear equilibrium density). The symbol np refers to matter with nucleons-only and npH to matter including hyperons.

FIG. 4.– Lepton chemical potentials in lepton-poor (left panel) and lepton-rich (right panel) matter at finite entropy as a function of baryon density n_B (n_0 is the nuclear equilibrium density). The symbol np refers to matter with nucleons-only and npH to matter including hyperons.

FIG. 5.– Binding energy as a function of baryon mass. The symbol np refers to matter with nucleons-only and npH to matter including hyperons at $T=0$ and $Y_\nu=0$.

FIG. 6.– Neutrino mean free paths in matter with nucleons only (left panels). Right panels show ratios of mean free paths in matter without and with hyperons. Abscissa is baryon density n_B (n_0 is the nuclear equilibrium density). Top panels show scattering mean free paths common to all neutrino species. The bottom panels show results for electron neutrino mean free paths where absorption reactions are included. The neutrino content is labelled

in the different panels.

FIG. 7.– Inverse neutrino mean free paths due to charged current reactions versus temperature.

Fig. 8.– Comparison of scattering mean free paths in neutrino poor matter at fixed entropy for different EOSs in matter containing nucleons and also hyperons.

FIG. 9.– Temporal variation of thermodynamic quantities (s : the entropy per baryon, T : the temperature, n_B : the baryon density, Y_ν : the net electron neutrino fraction, μ_ν : electron neutrino chemical potential, and Y_e : the net electron concentration) inside a star for the baseline GM3 model for nucleons-only matter. Labels indicate time in seconds. The abscissa shows the enclosed baryonic mass.

FIG. 10.– Typical electron-neutrino and muon-neutrino mean free paths. For the electron neutrino the average energy $\langle E_\nu \rangle = \mu_{\nu_e} + \pi T$, while for the muon and tau neutrinos $\langle E_\nu \rangle = \pi T$. Top panels show temporal variations for the baseline GM3 model in nucleons-only matter and the bottom panels show results in matter including hyperons.

FIG. 11.– Effects of changing initial entropy profiles. Results of the baseline GM3 model (solid curves) with nucleons only with an initial $s \sim 1$ in the core are compared to those (dashed curves) of a model with reduced initial entropy in the core ($s \sim 0.5$). Symbols as in Figure 9.

FIG. 12.– Effects of changing initial entropy profiles. Results of the baseline GM3 model (solid curves) with nucleons only with an initial $s \sim 1$ in the core are compared to those (dashed curves) of a model with an enhanced initial entropy in the core ($s \sim 2$). The dotted curves show effects of enhancing the entropy in the surface regions. Symbols as in Figure 9.

FIG. 13.– Effects of changing initial lepton profiles. Results of the baseline GM3 model (solid curves) with nucleons only with an initial $Y_L \cong 0.38$ in the core are compared to those (dashed curves) of a model with an enhanced initial lepton content in the core ($Y_L \cong 0.4$). Symbols as in Figure 9.

FIG. 14.– Comparison of total neutrino energy luminosity versus time between the baseline model and different initial models.

FIG. 15.– Temporal variation of the entropy, temperature and baryon density in matter containing nucleons only (left panels) and in matter that also contains hyperons (right panels). Differences arising from the underlying EOS are apparent by comparing the solid and dashed curves. The abscissa shows the enclosed baryonic mass in a $1.6M_\odot$ star.

FIG. 16.– Temporal variation of the net electron neutrino fraction, electron neutrino chemical potential, and the net electron concentration in matter containing nucleons only (left panels) and in matter that also contains hyperons (right panels). Differences arising from the underlying EOS are apparent by comparing the solid and dashed curves. The abscissa shows the enclosed baryonic mass in a $1.6M_\odot$ star.

FIG. 17.– Effects of changing the underlying EOS (GM1 versus GM3) on the core values of the thermodynamic quantities versus time in matter containing nucleons only (thin solid and dashed curves) and in matter that also contains hyperons (thick solid and dashed curves). Results are for a $M_B = 1.6M_\odot$ star.

FIG. 18.– Comparison of the mean neutrino energy (top panels) and the total neutrino energy luminosity (bottom panels) versus time for the different EOS models. The left panels show results for a baryon mass $M_B = 1.6M_\odot$ and the right panels for a baryon mass

$$M_B = 1.8M_\odot.$$

FIG. 19.– Temporal evolution of strangeness per baryon for the indicated baryon masses.

FIG. 20.– Mass dependence of the core values of the thermodynamic quantities versus time in matter containing nucleons only (solid curves) and in matter that also contains hyperons (dashed curves).

FIG. 21.– Mass dependence of the average energy of the emitted neutrinos (top panels) and the total neutrino energy luminosity (bottom panels) in models with and without hyperons.

FIG. 22.– Top panel: Evolution of the central baryon number density for different baryonic mass stars containing hyperons (model GM3npH) which are metastable. Bottom panel: Time required by stars shown in the top panel to reach the unstable configuration.

FIG. 23.– Evolution of (GM_G/Rc^2) in a $M_B = 1.88M_\odot$ star containing hyperons (model GM3npH). Inset labels show time in seconds.

FIG. 24.– Evolution of convectively unstable regions in a $M_B = 1.6M_\odot$ star. Top panel shows results for a star containing nucleons only and the bottom panel is for a star that also contains hyperons.

FIG. 25.– Neutrino signals in terrestrial detectors KII and IMB, and for a supernova at 50 kpc. Top panels show total number of counts, and the bottom panels show the count rate. Left panels are for $M_B=1.6 M_\odot$, and right panels show results for $M_B=1.8 M_\odot$.

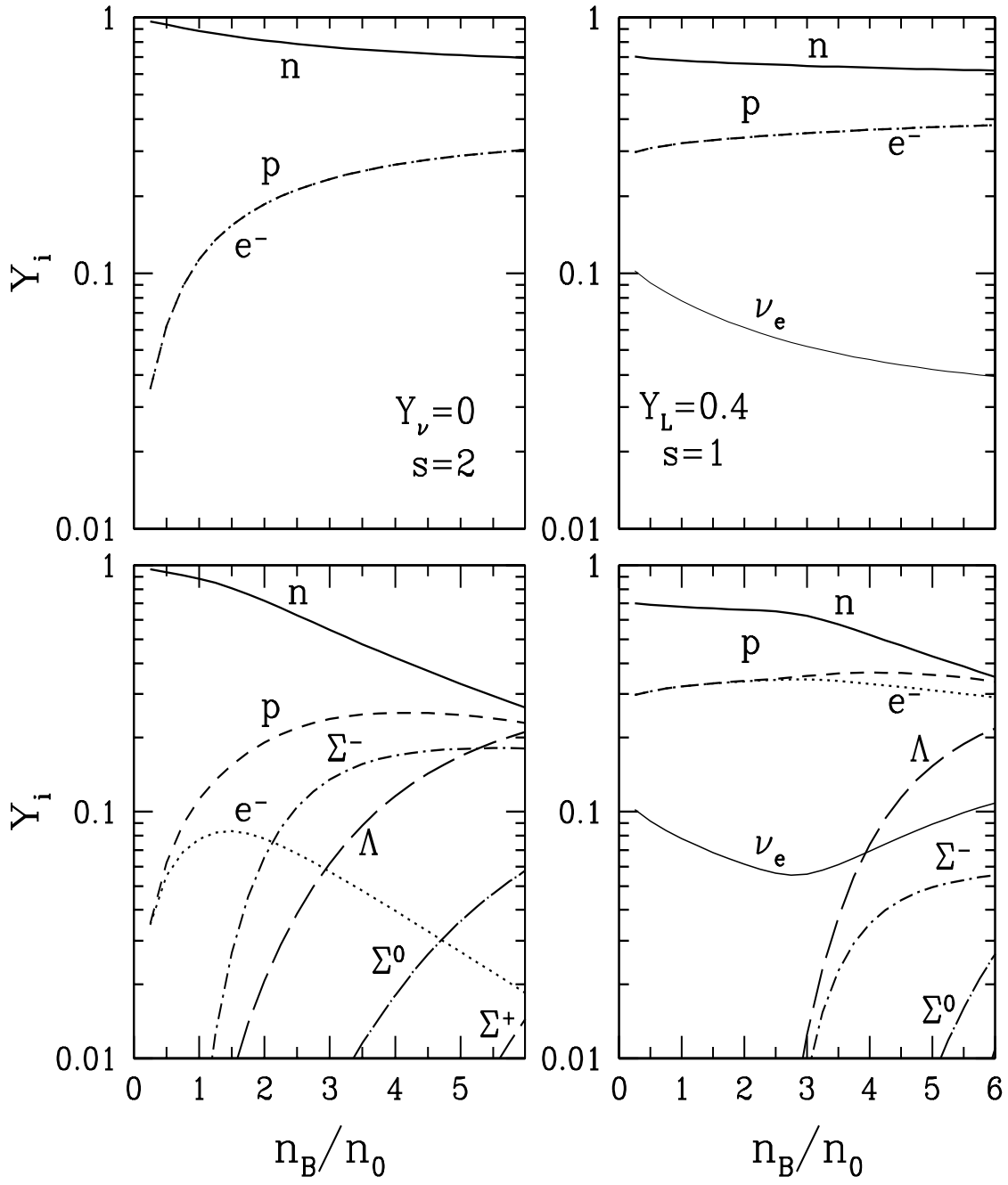


Fig. 1.—

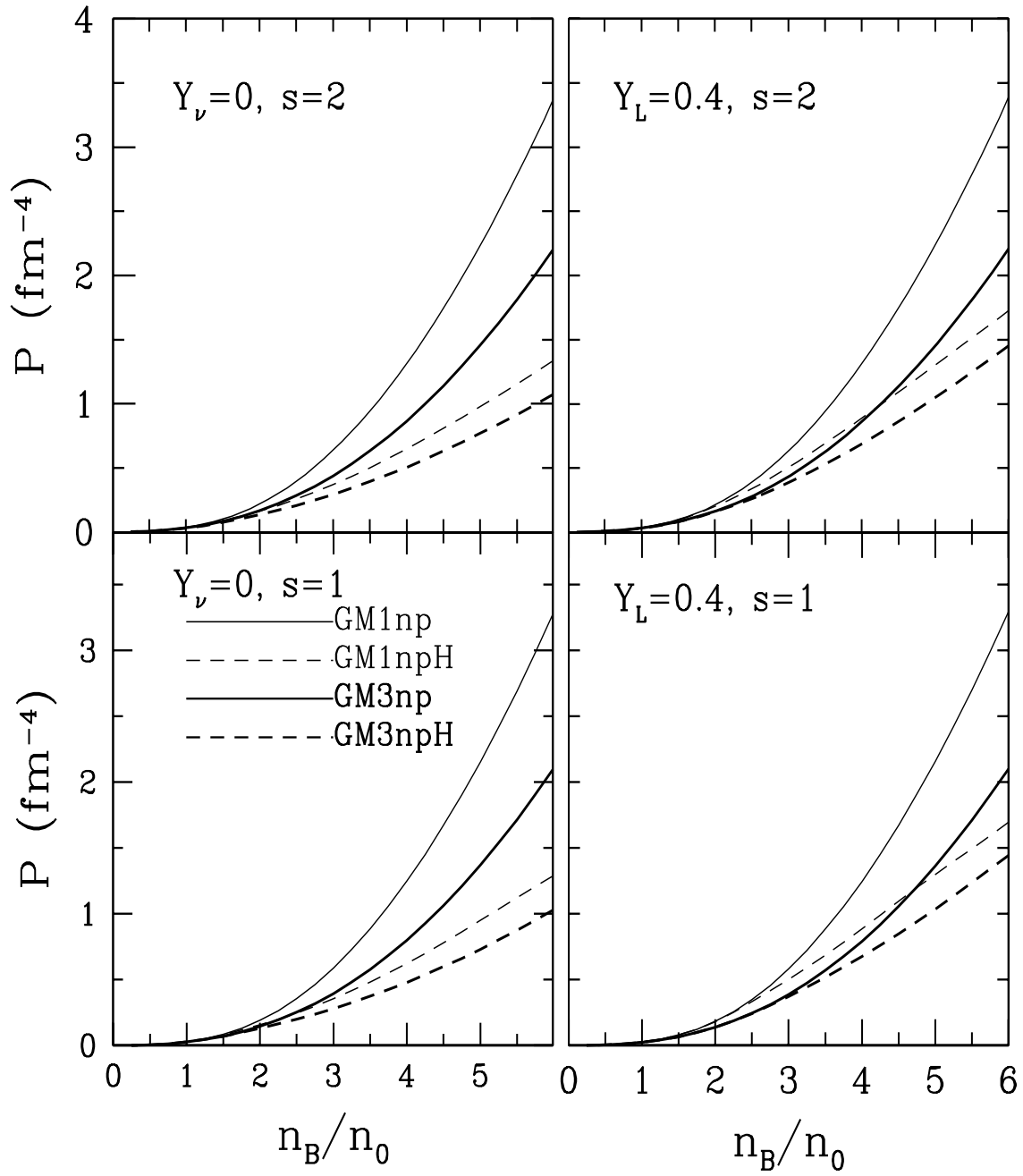


Fig. 2.—

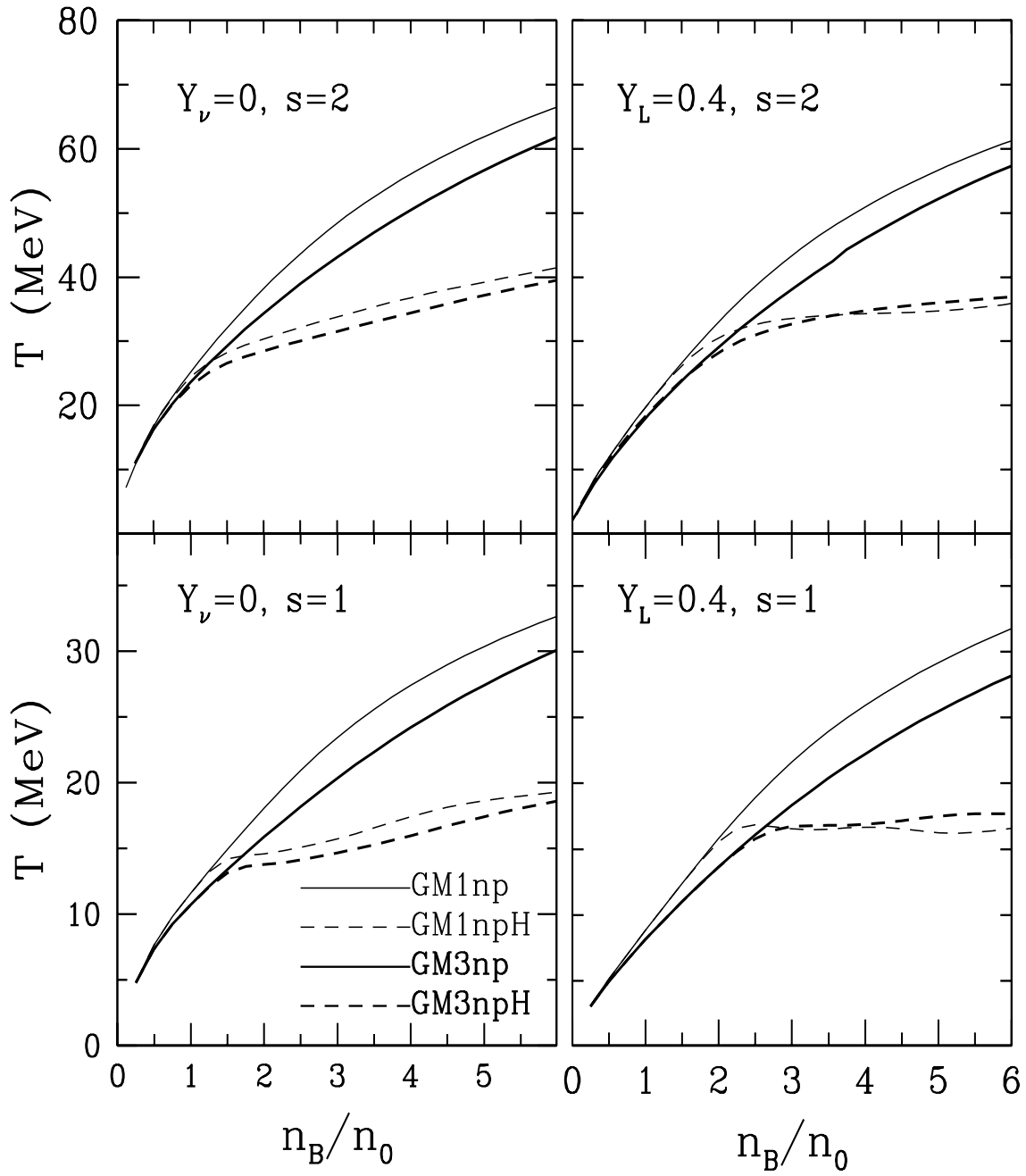


Fig. 3.—

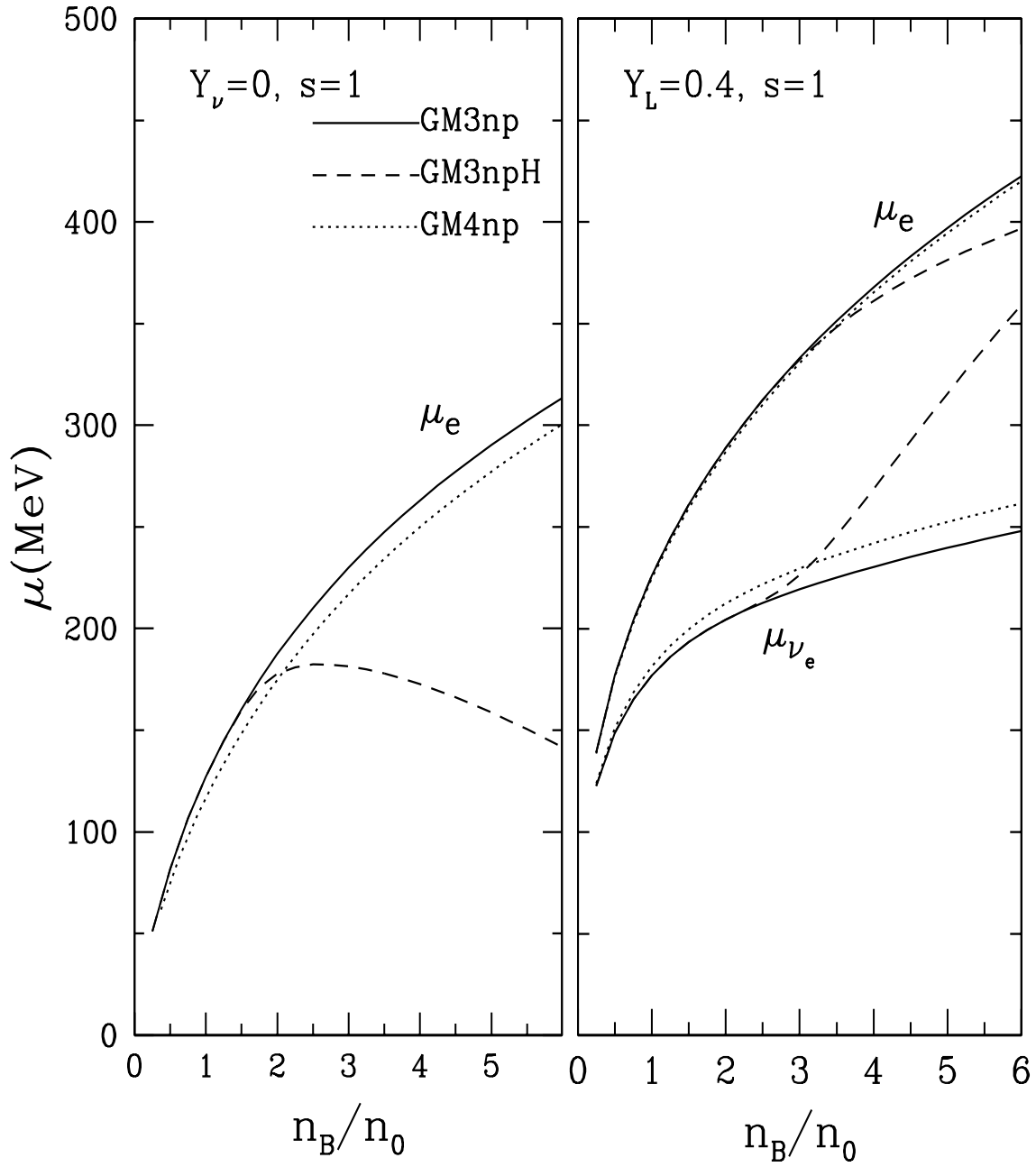


Fig. 4.—

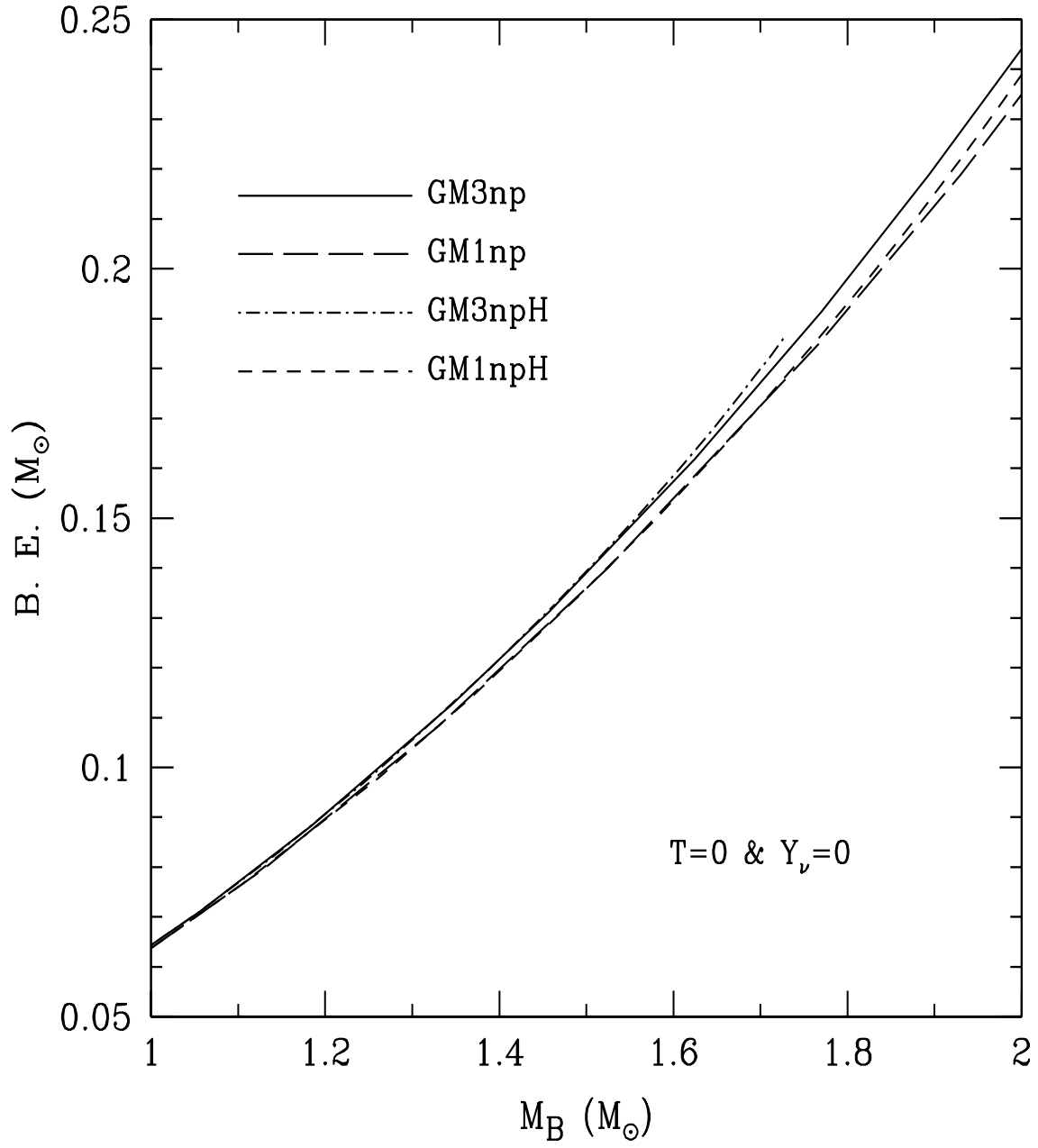


Fig. 5.—

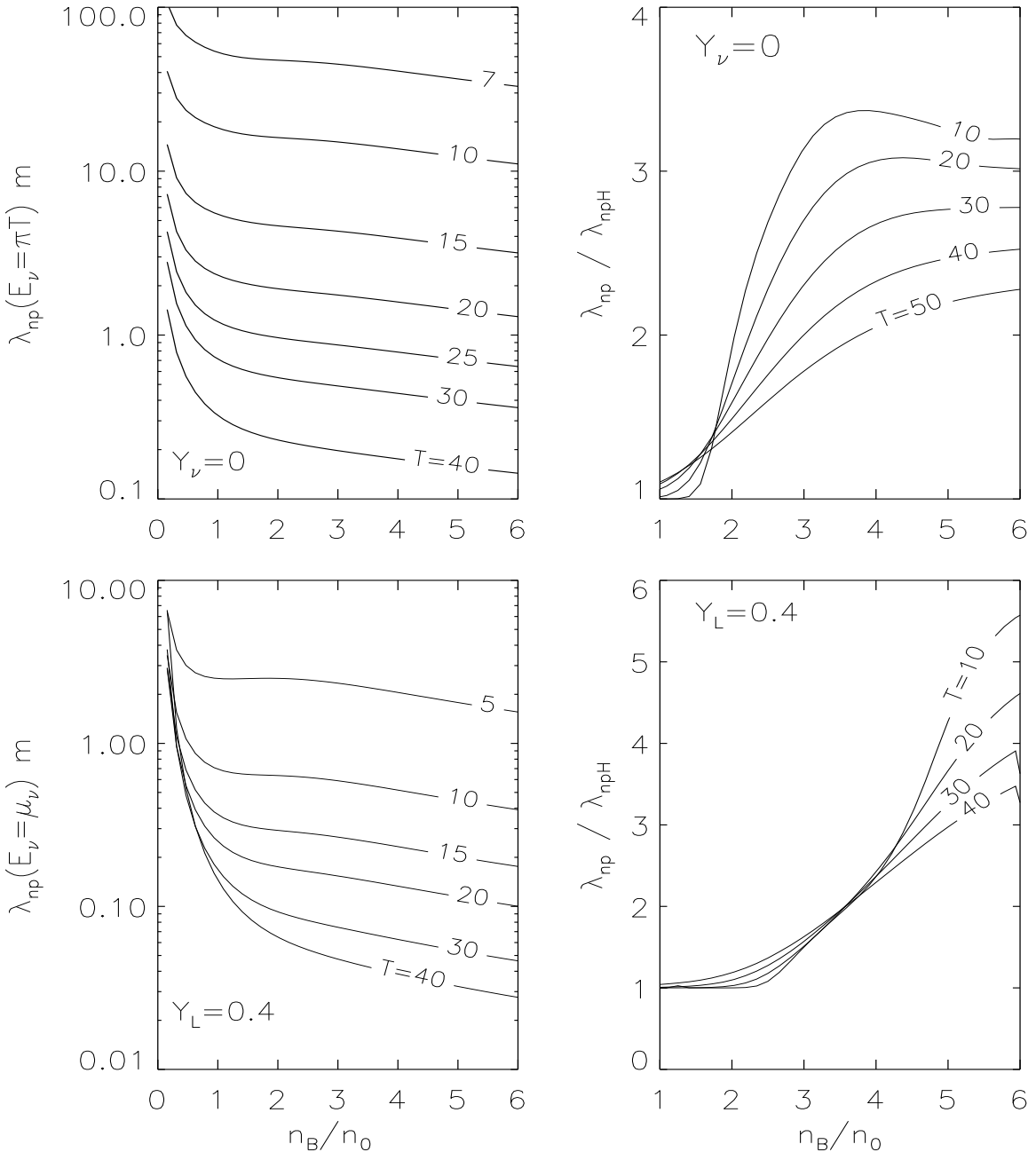


Fig. 6.—

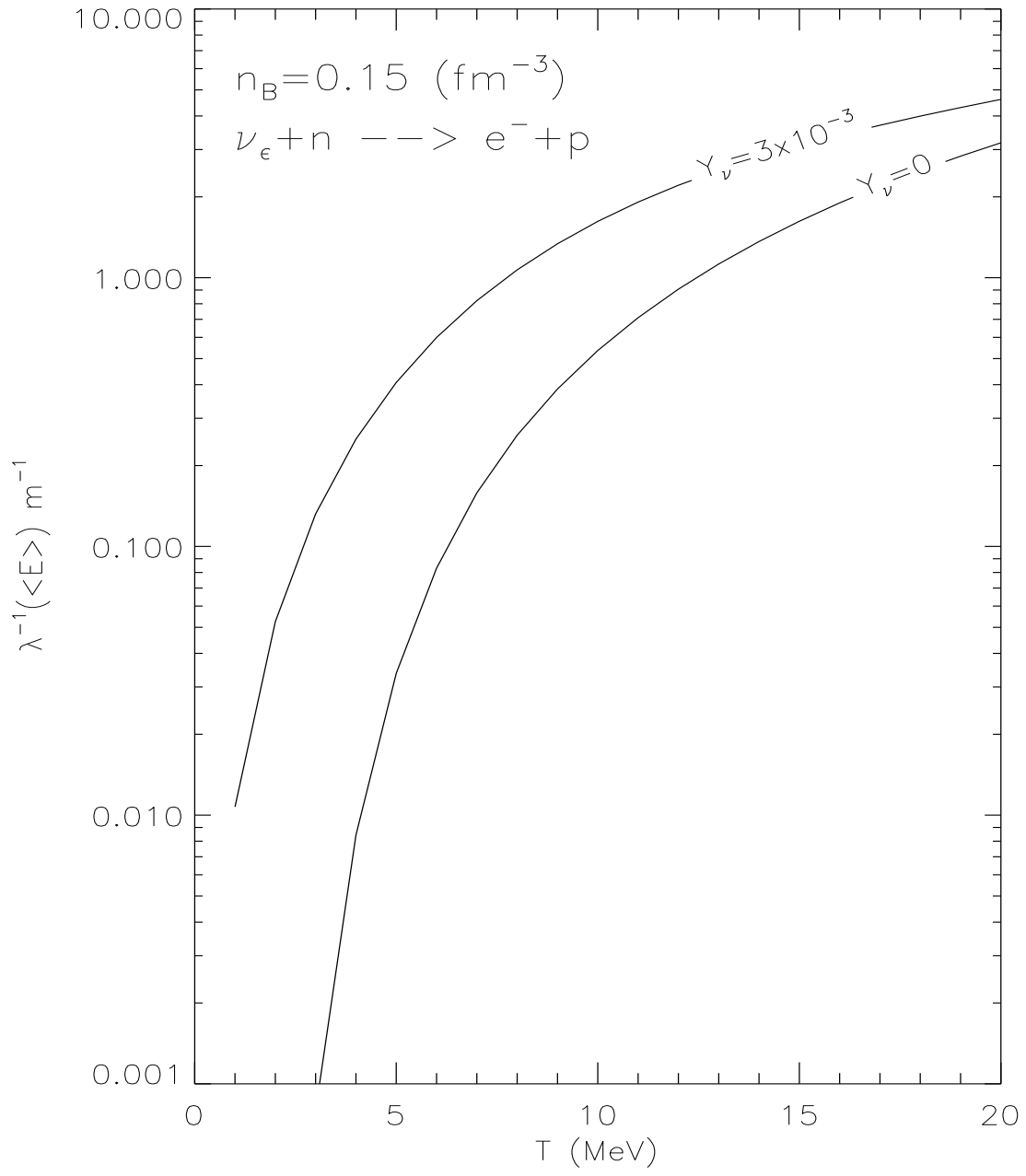


Fig. 7.—

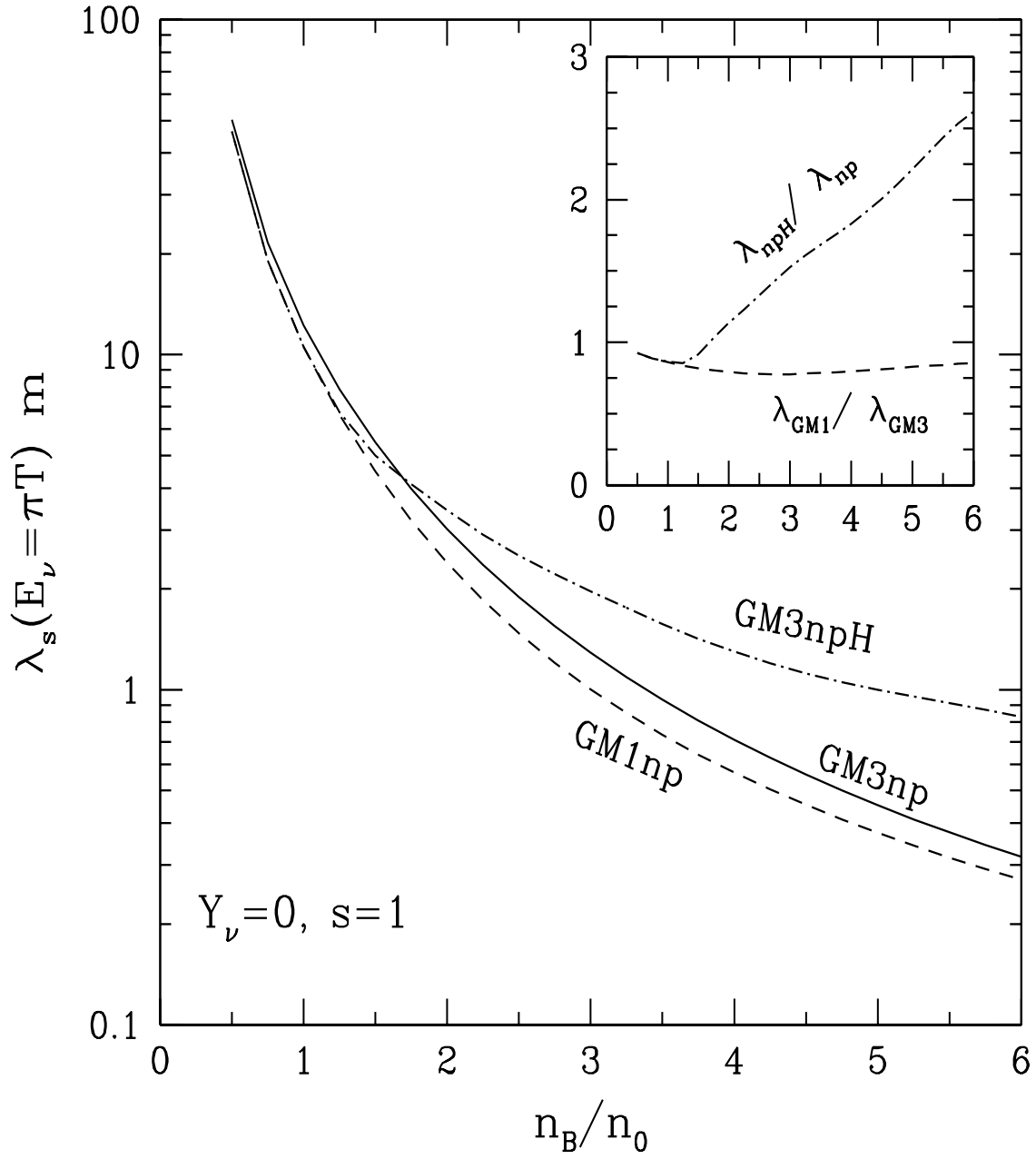


Fig. 8.—

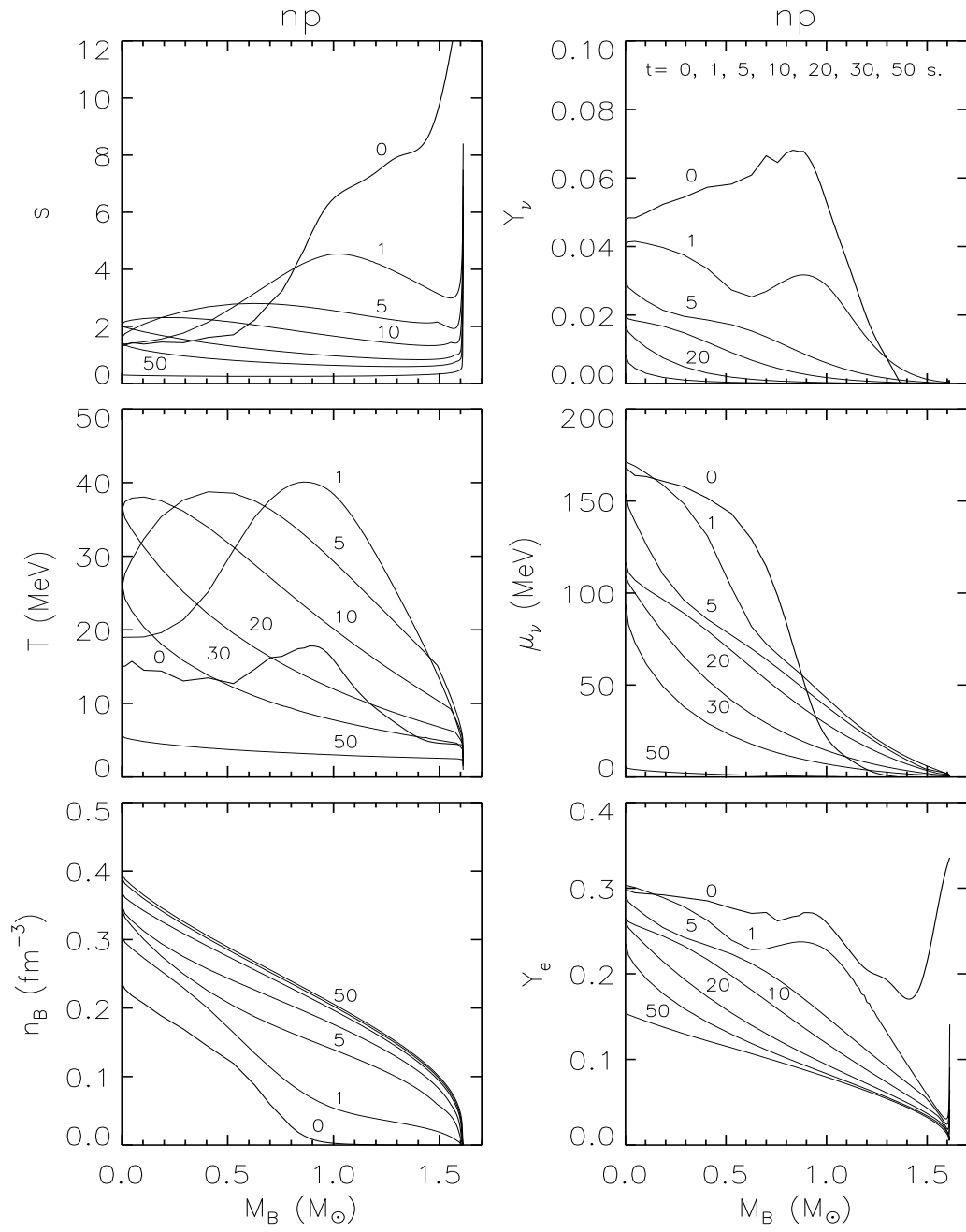


Fig. 9.—

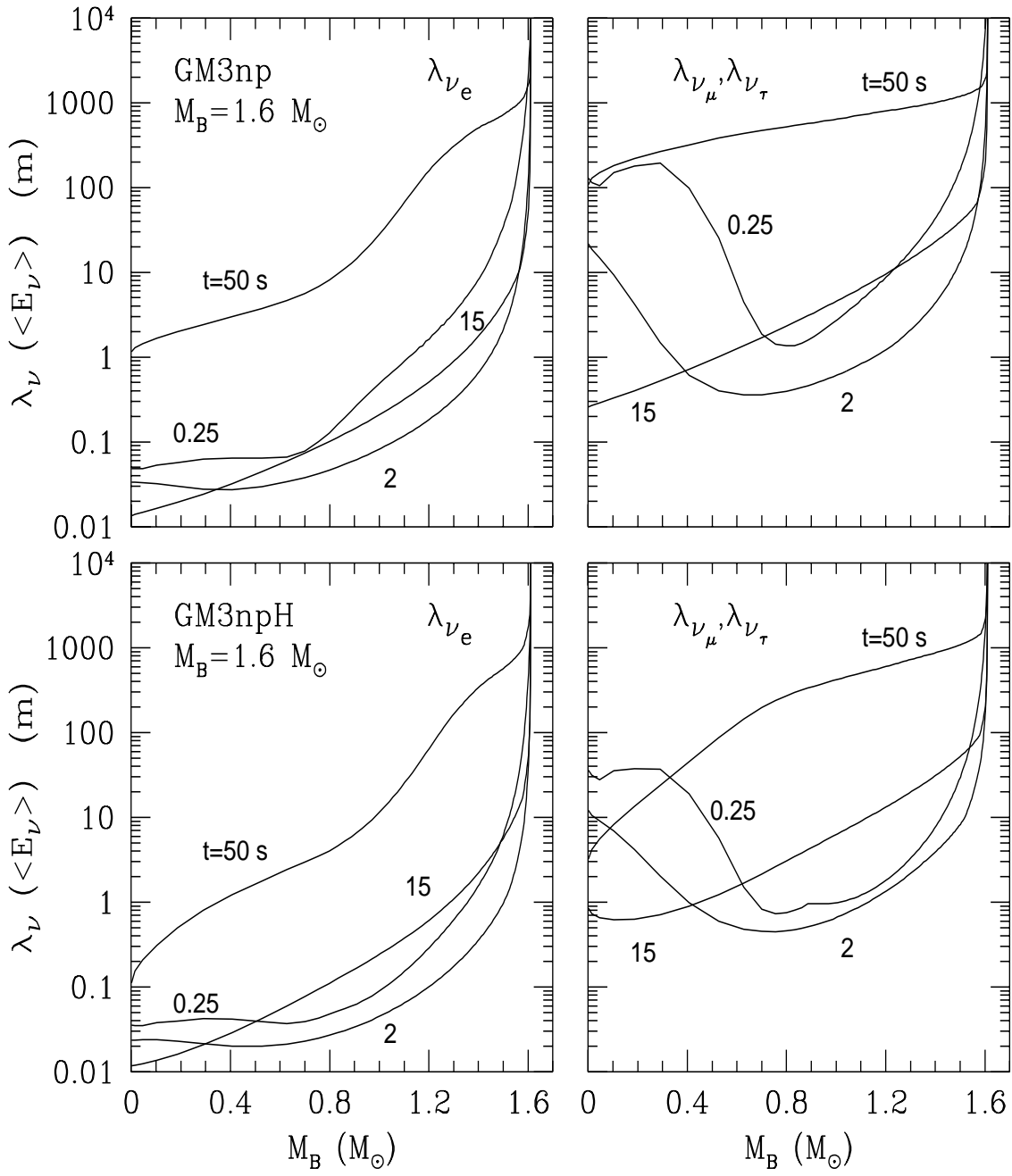


Fig. 10.—

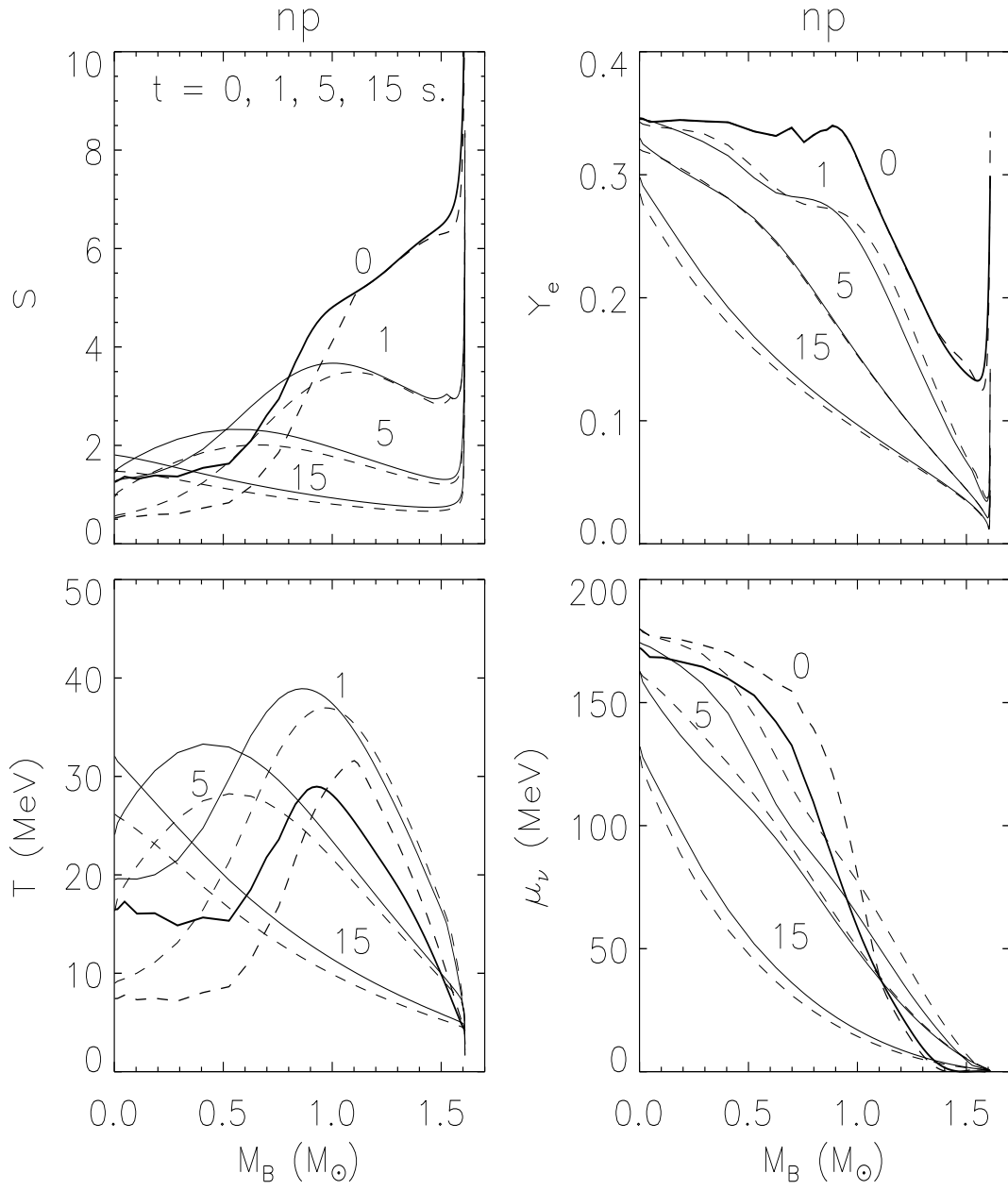


Fig. 11.—

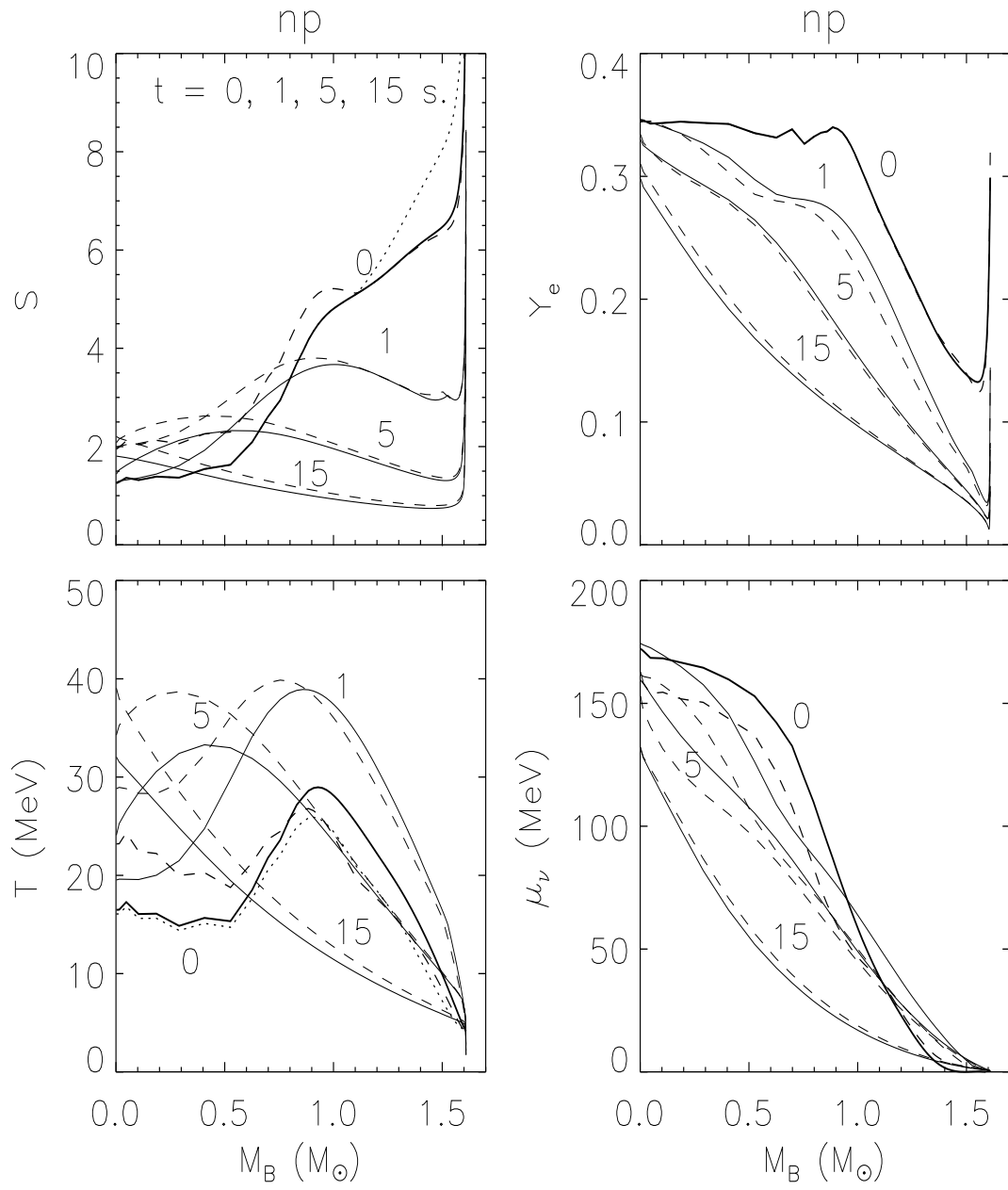


Fig. 12.—

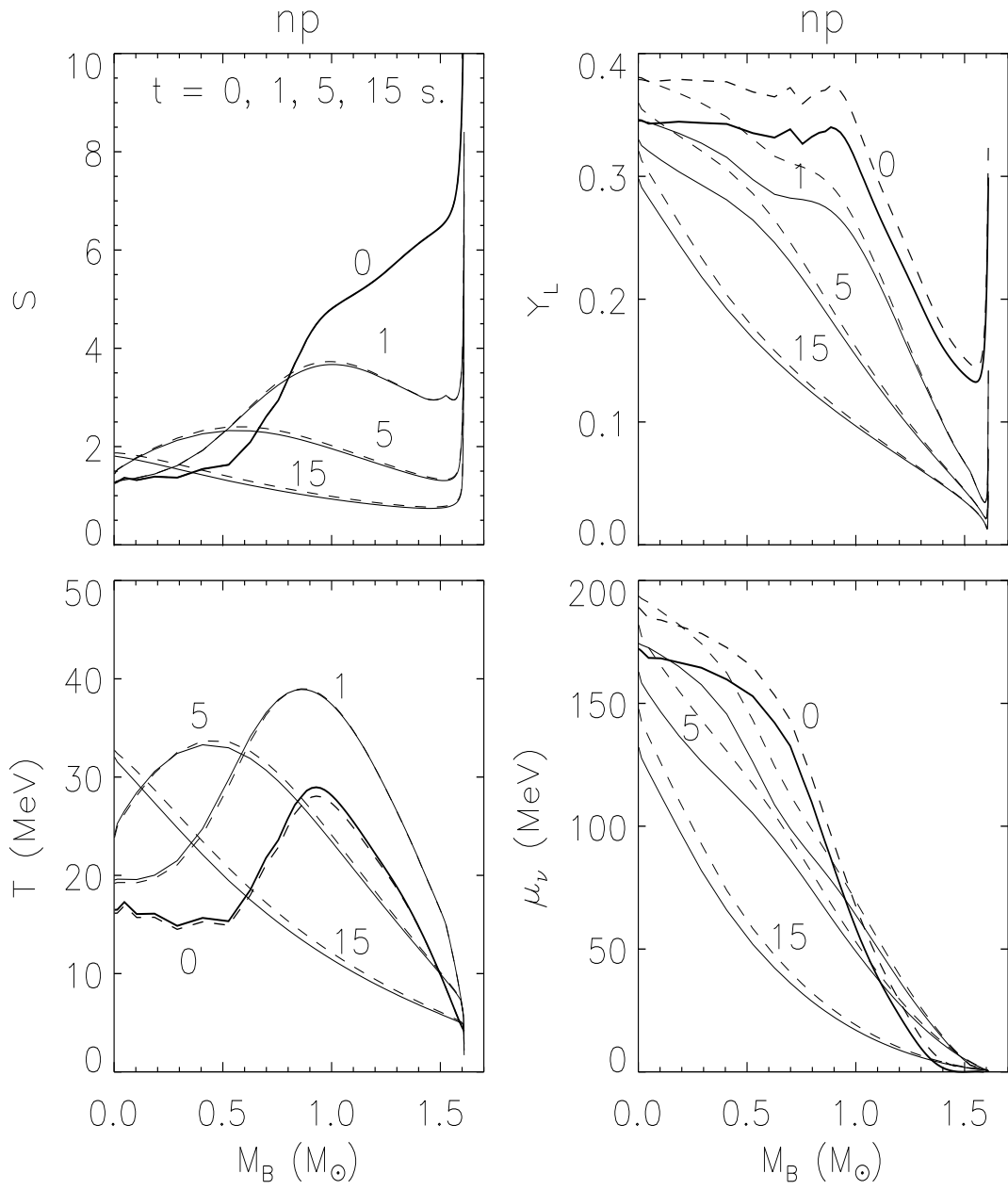


Fig. 13.—

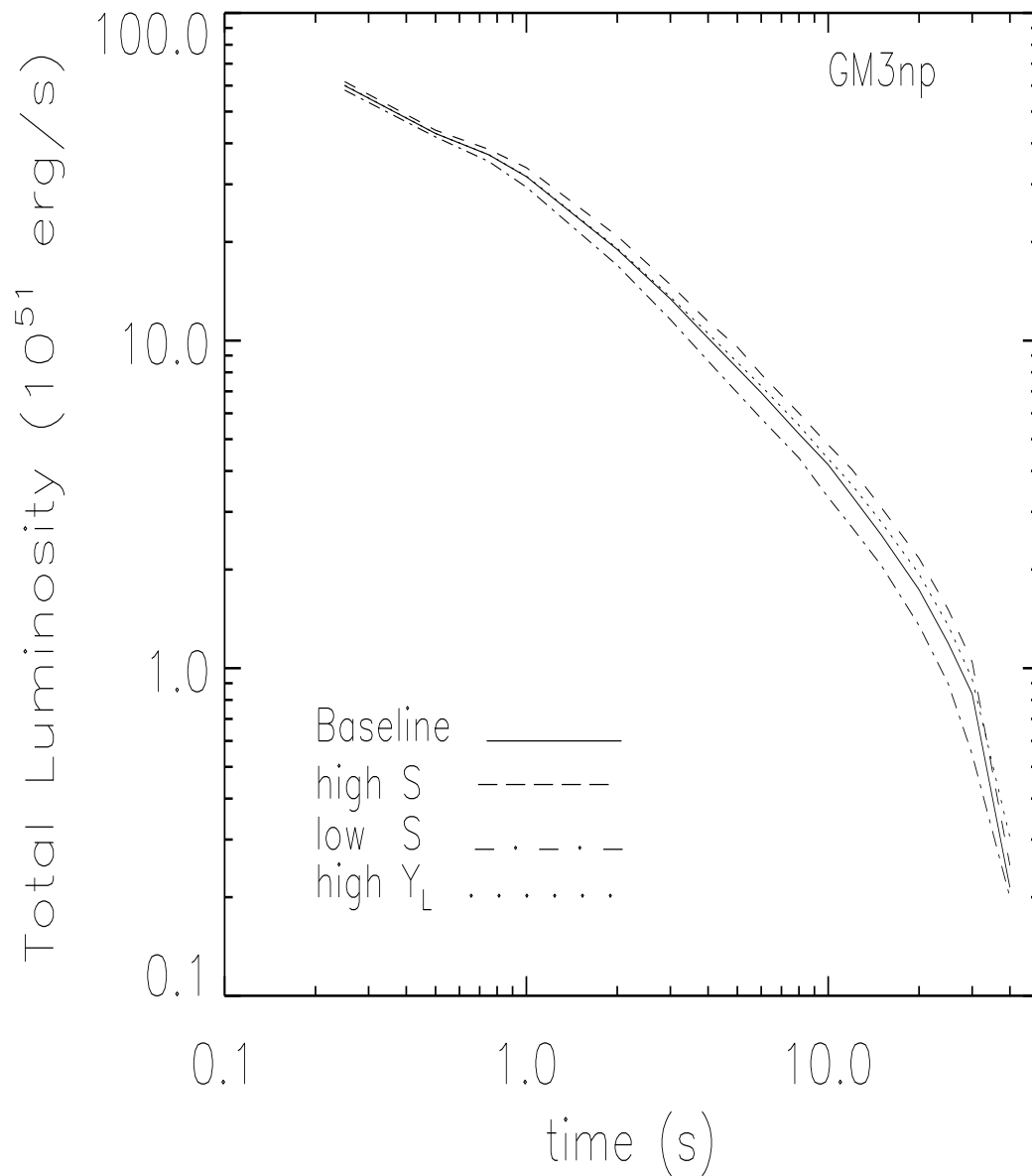


Fig. 14.—

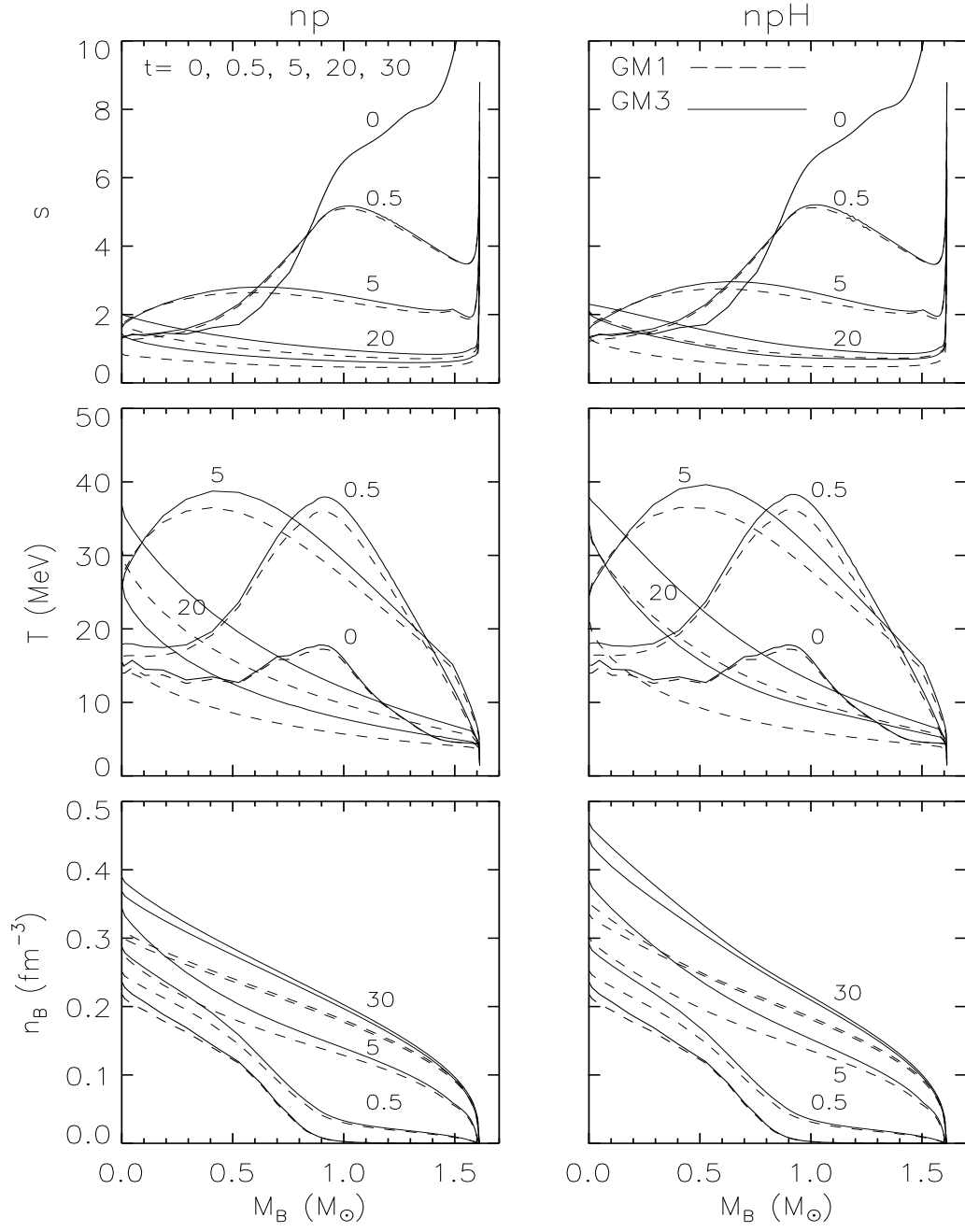


Fig. 15.—

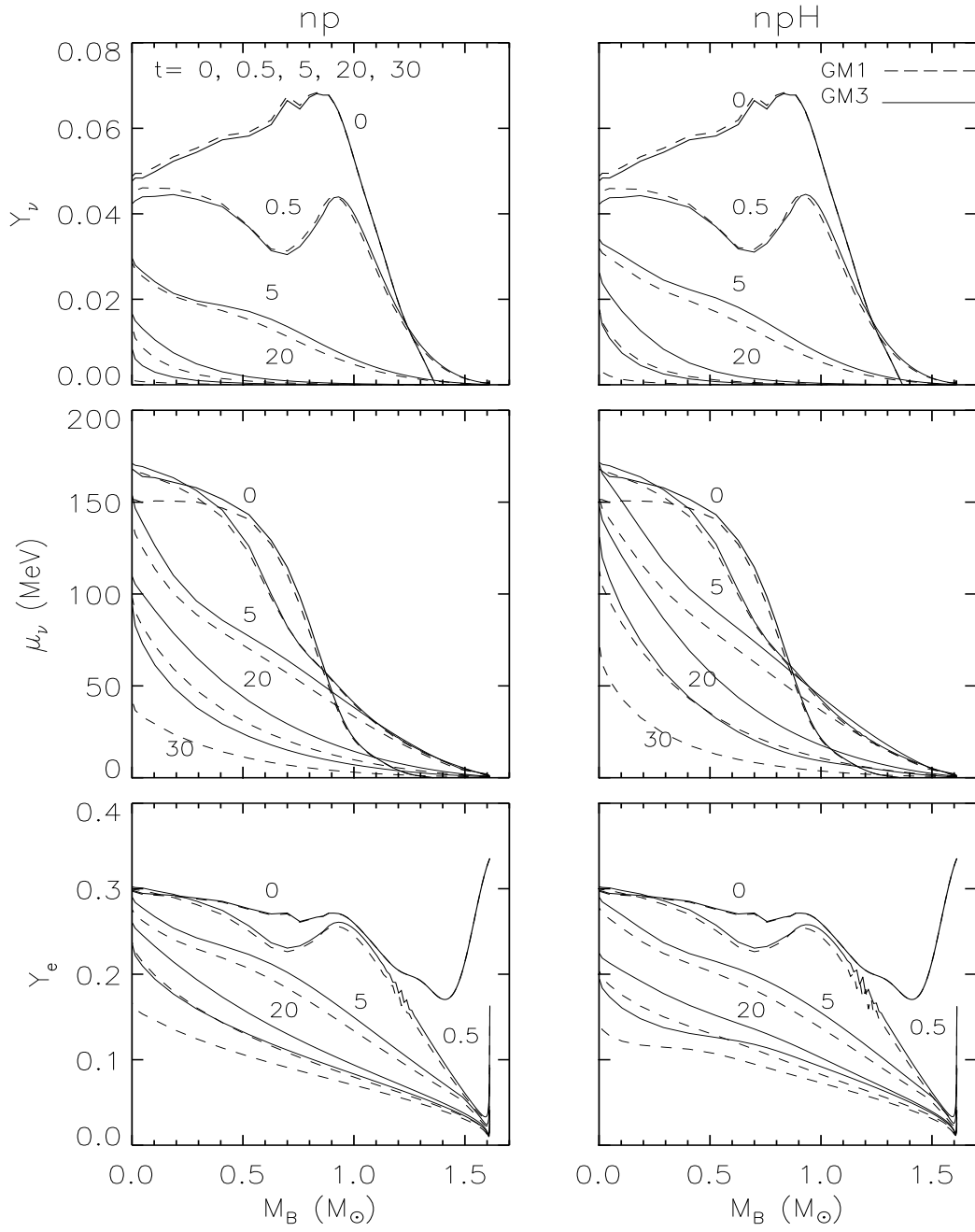


Fig. 16.—

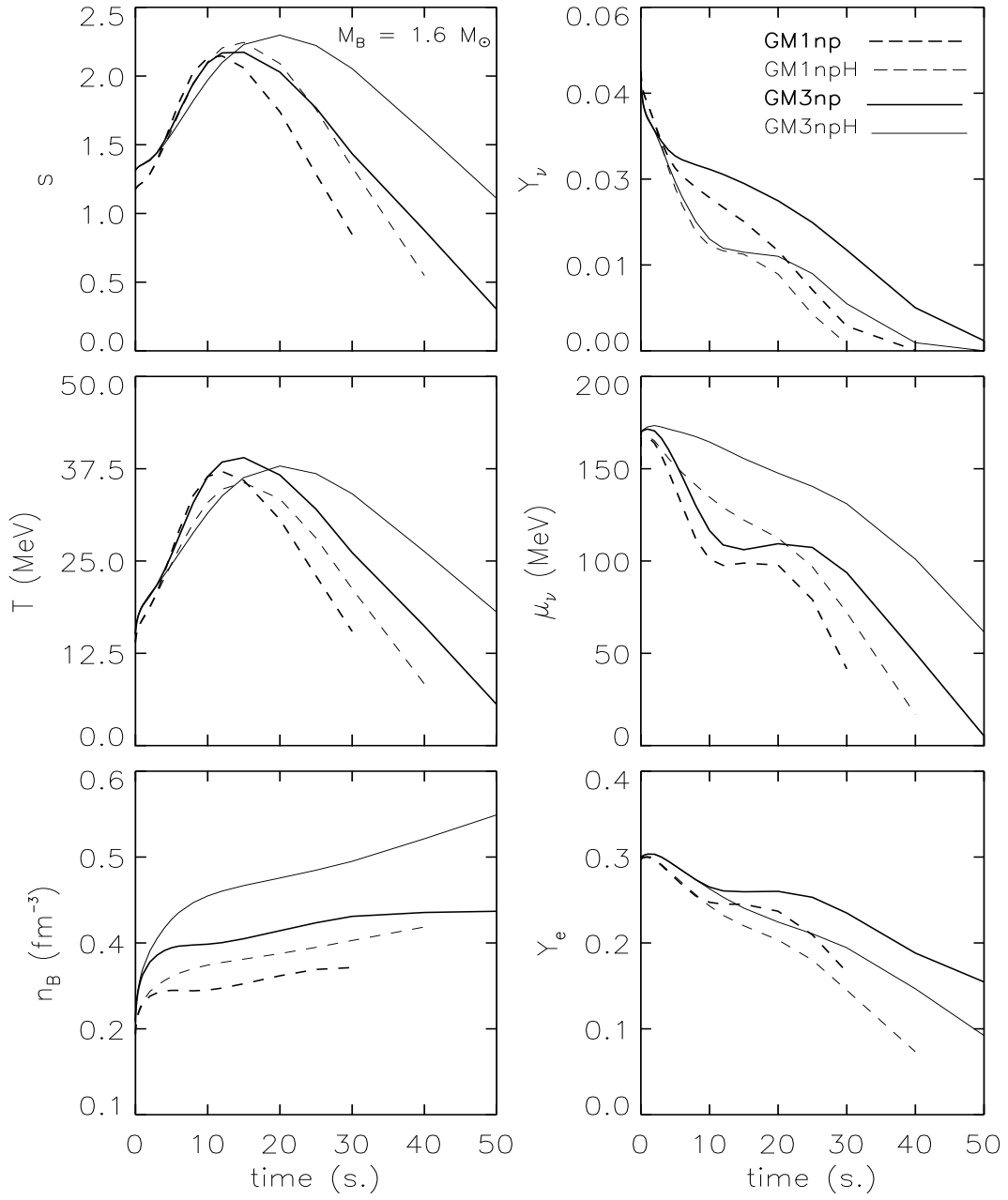


Fig. 17.—

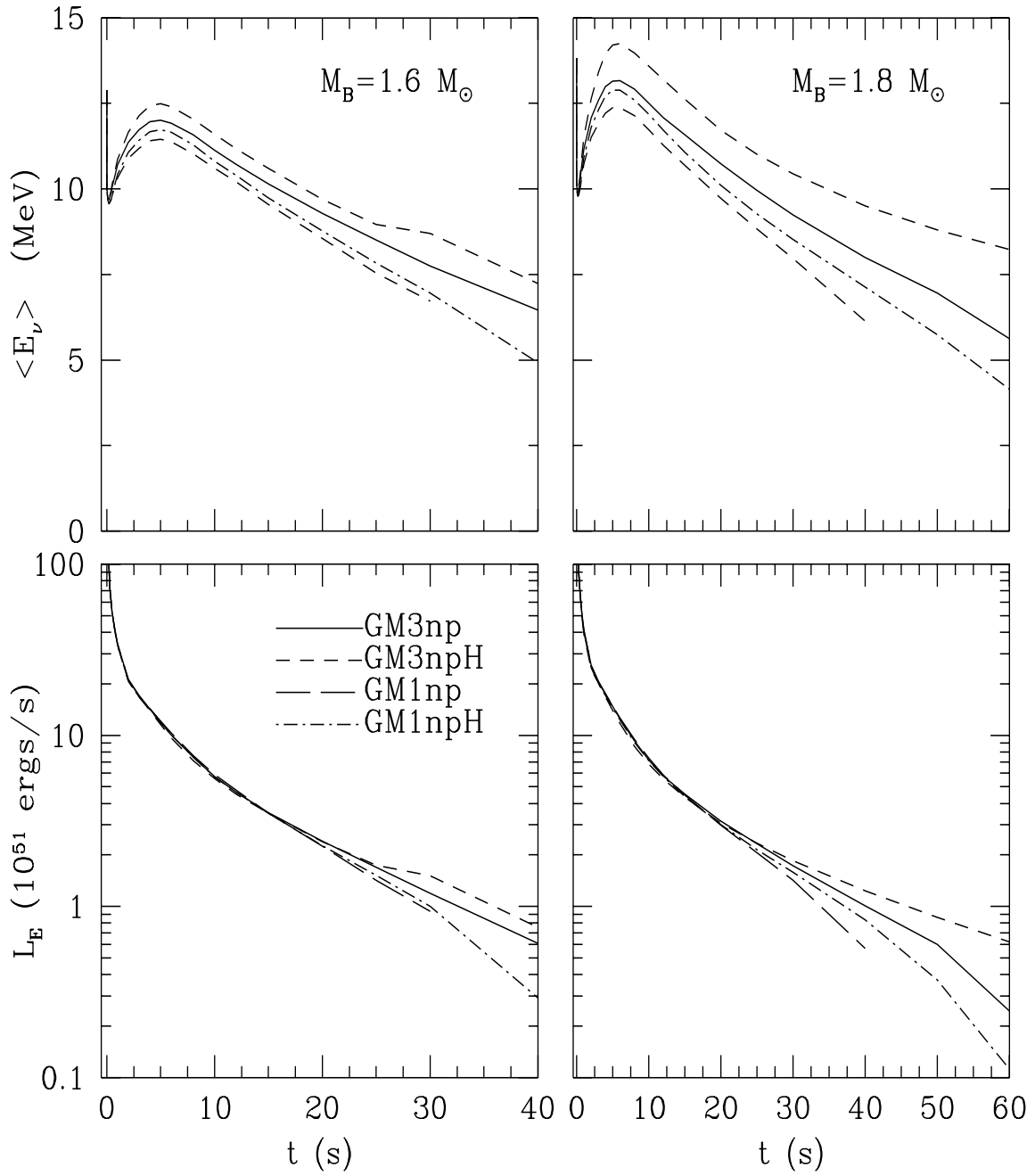


Fig. 18.—

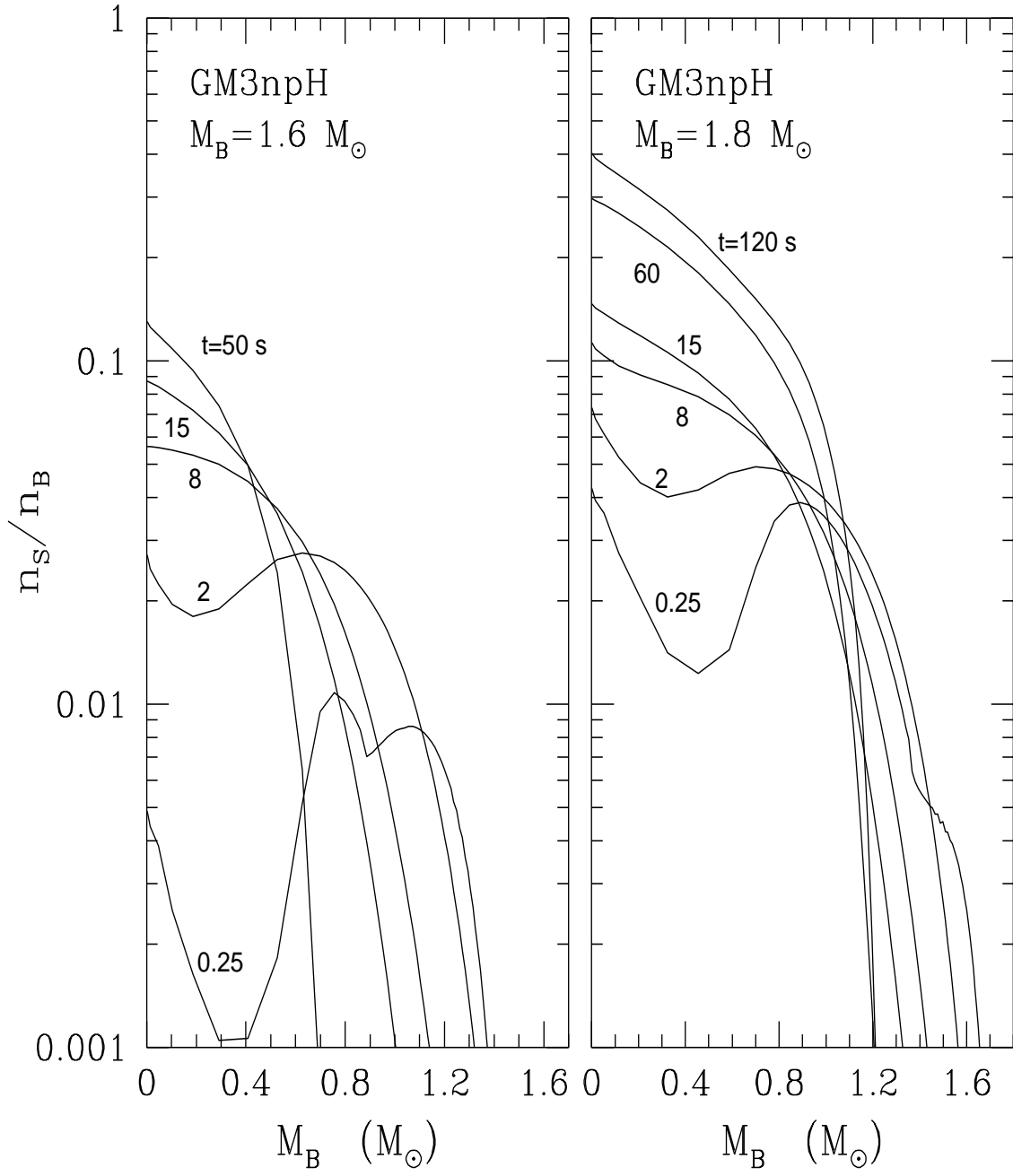


Fig. 19.—

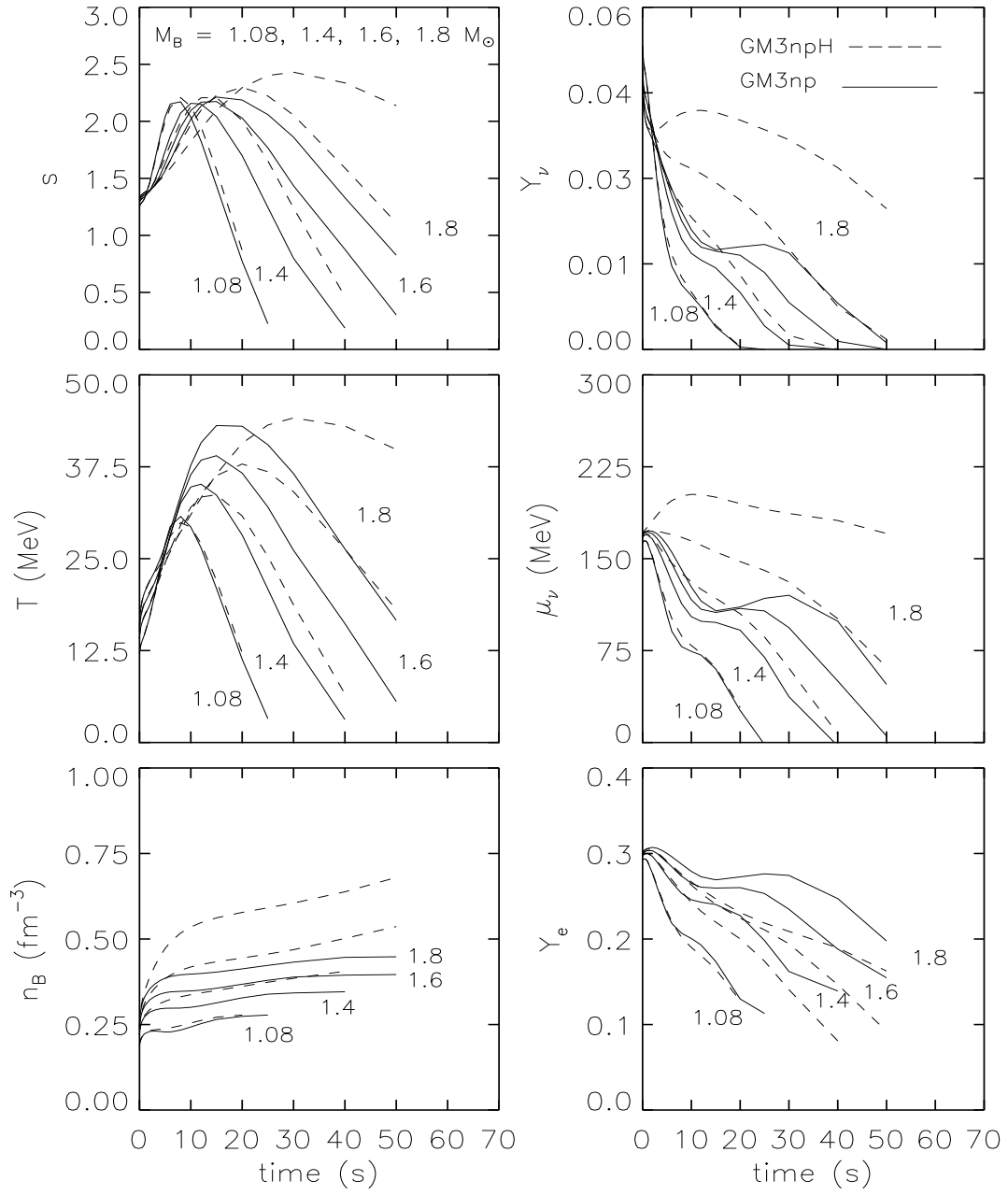


Fig. 20.—

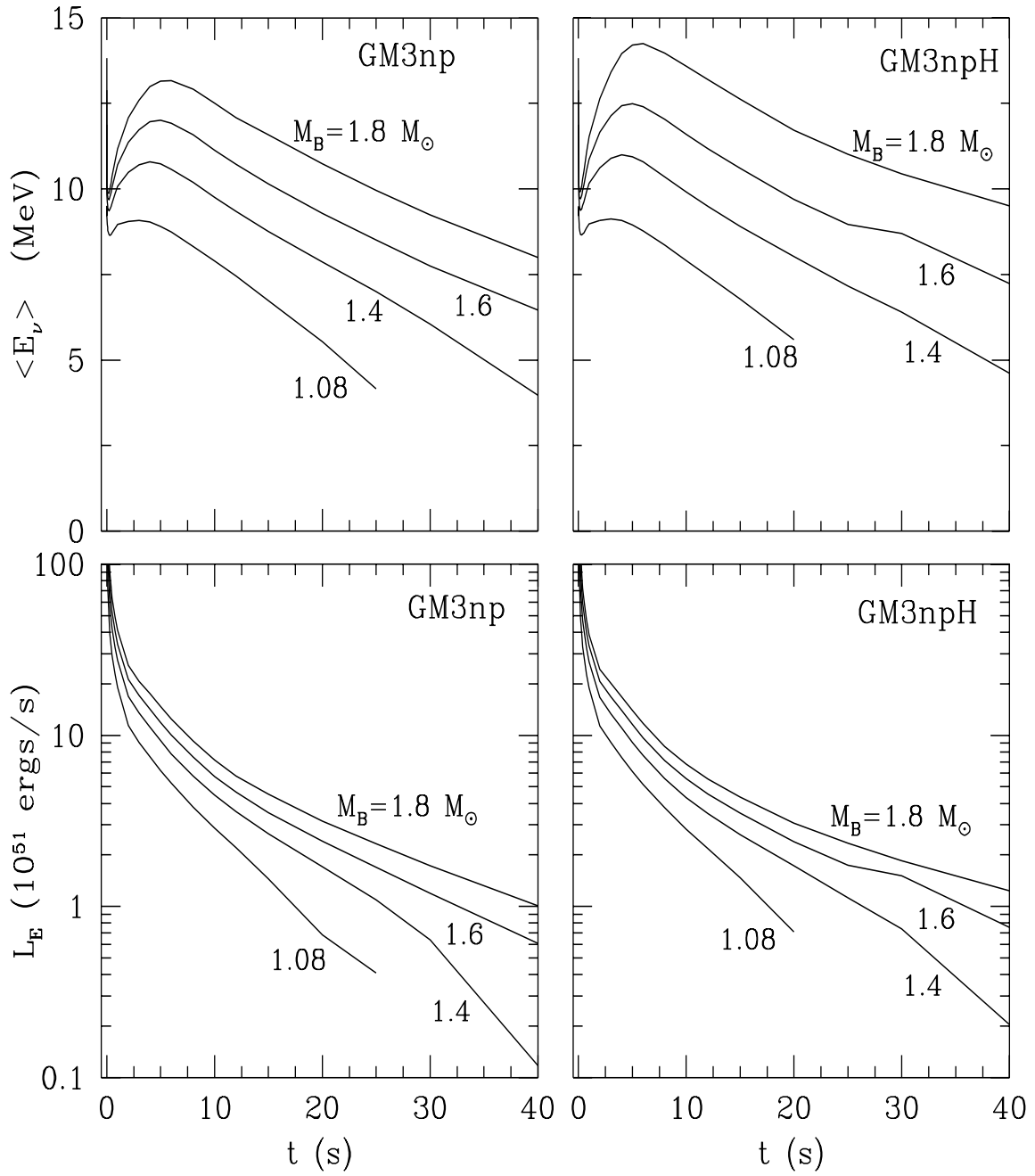


Fig. 21.—

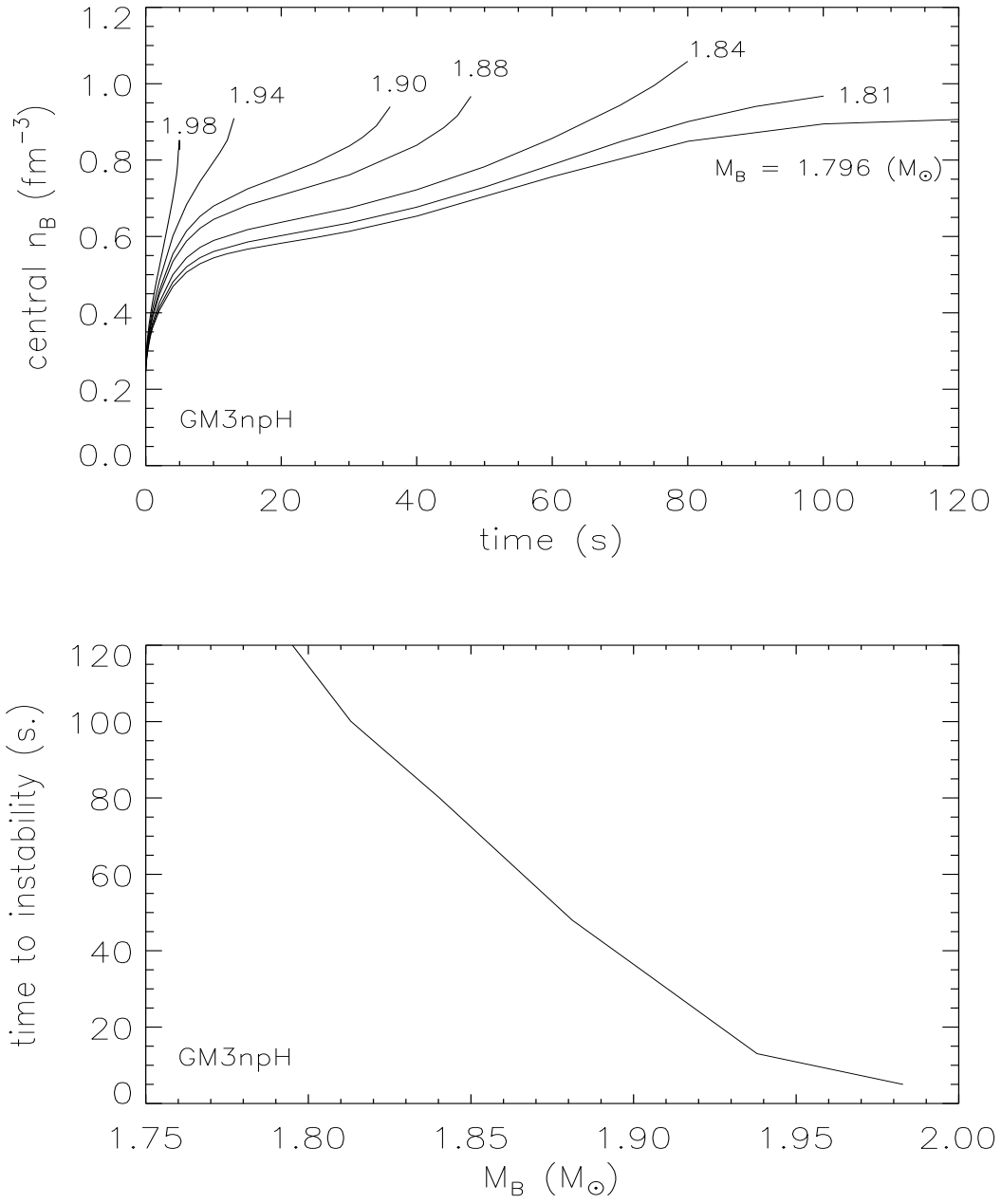


Fig. 22.—

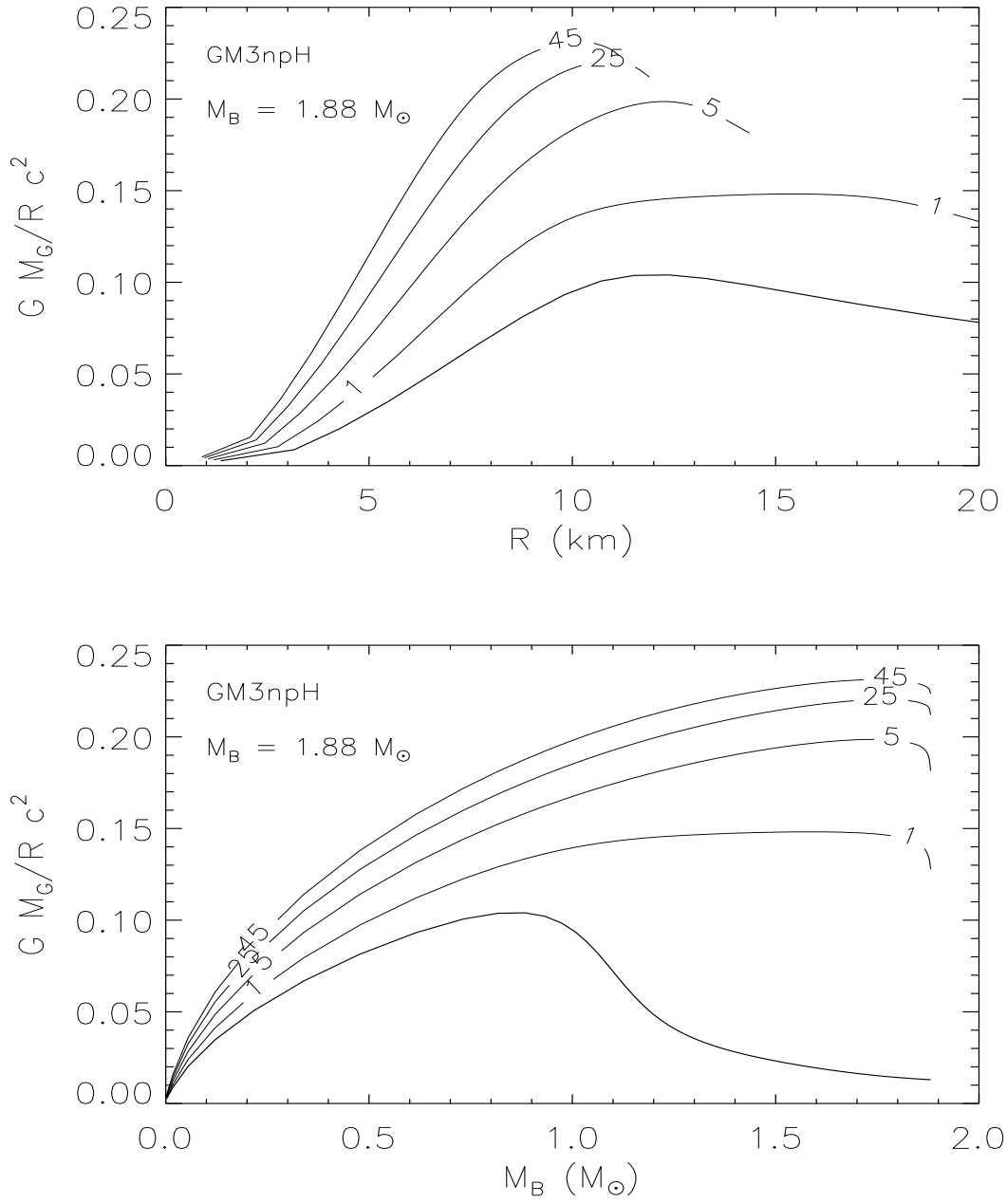


Fig. 23.—

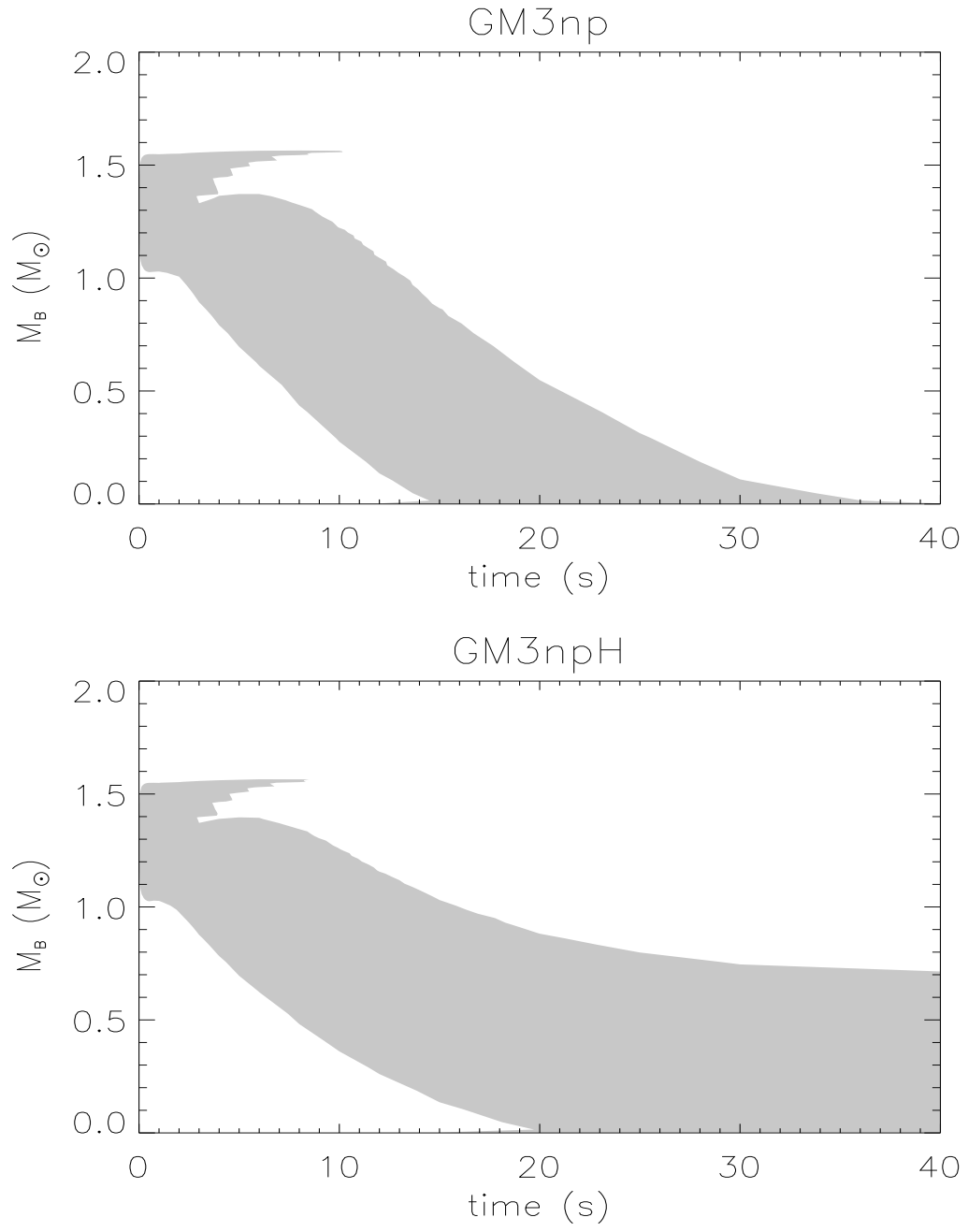


Fig. 24.—

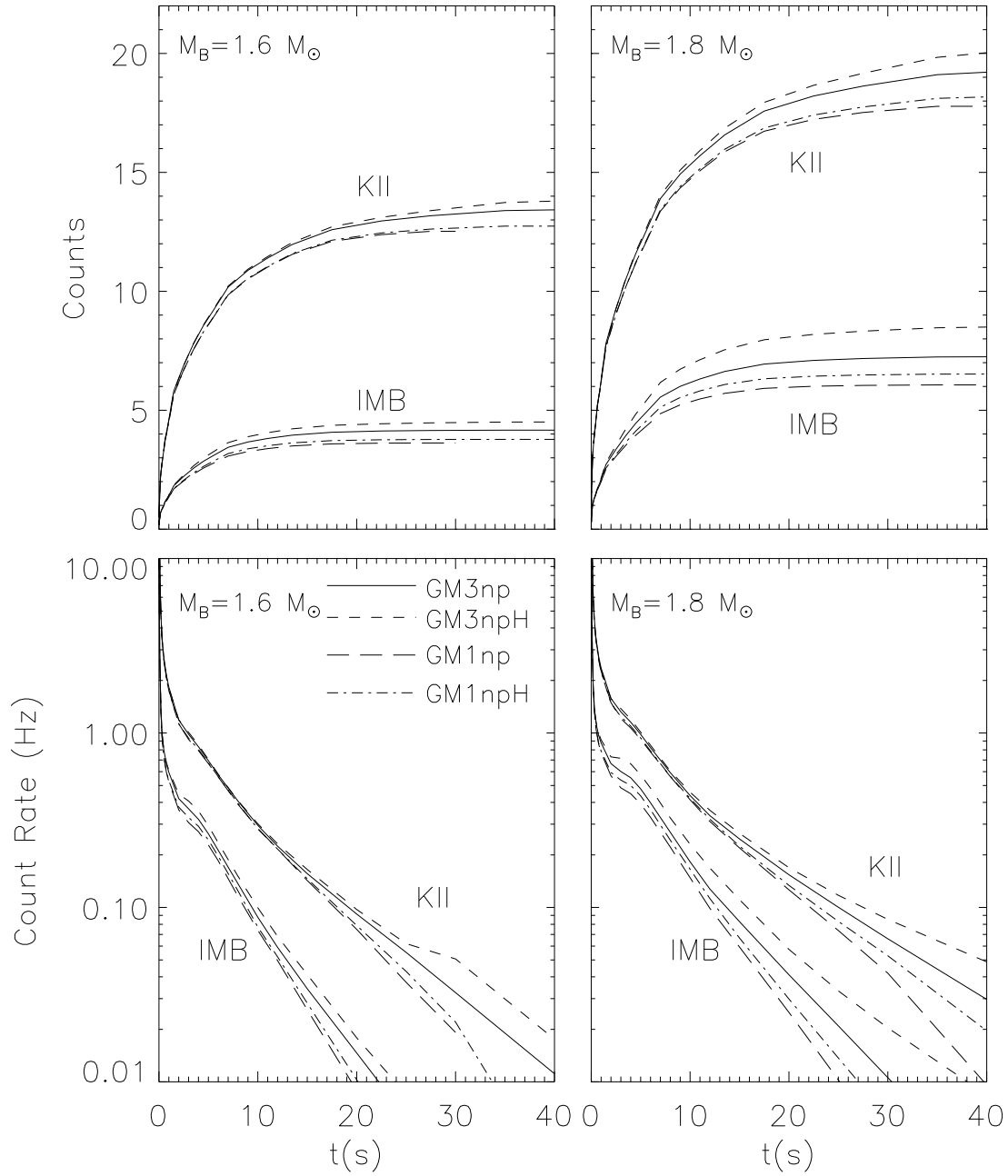


Fig. 25.—